

All-sky aerosol direct radiative effects at the ARM SGP site

K. A. Balmes, Q. Fu

Department of Atmospheric Sciences, University of Washington, Seattle, WA, USA

Key Points:

- All-sky aerosol direct radiative effect (DRE) was estimated using multi-year ground-based observations at ARM SGP site for the first time
- The annual mean all-sky aerosol DRE at the top of the atmosphere (TOA) is $-2.13 \pm 0.54 \text{ W m}^{-2}$, compared to $-3.00 \pm 0.58 \text{ W m}^{-2}$ for clear-skies
- The relative uncertainty in estimated all-sky TOA aerosol DRE due to aerosol single-scattering albedo errors is larger than for clear-skies

Corresponding author: K. A. Balmes, kbalmes@uw.edu

This article has been accepted for publication and undergone full peer review but has not been through the copyediting, typesetting, pagination and proofreading process, which may lead to differences between this version and the [Version of Record](#). Please cite this article as [doi: 10.1029/2021JD034933](https://doi.org/10.1029/2021JD034933).

This article is protected by copyright. All rights reserved.

Abstract

All-sky aerosol direct radiative effect (DRE) was estimated for the first time at the Atmospheric Radiation Measurement Southern Great Plains site using multi-year ground-based observations. The NASA Langley Fu-Liou radiation model was employed. Observed inputs for the radiation model include aerosol and cloud vertical extinction profile from Raman lidar; spectral aerosol optical depth, single-scattering albedo, and asymmetry factor from Aerosol Robotic Network; cloud water content profiles from radars; temperature and water vapor profiles from radiosondes; and surface shortwave spectral albedo from radiometers. A cloudy-sky radiative closure experiment was performed. The relative mean differences between modeled and observed surface downwelling shortwave total fluxes were 6% (7%) for transparent (opaque) cloudy-skies. The estimated annual mean all-sky aerosol DRE is $-2.13 \pm 0.54 \text{ W m}^{-2}$ at the top of atmosphere (TOA) and $-5.95 \pm 0.87 \text{ W m}^{-2}$ at the surface, compared to $-3.00 \pm 0.58 \text{ W m}^{-2}$ and $-6.85 \pm 1.00 \text{ W m}^{-2}$, respectively, under clear-sky conditions. The seasonal cycle of all-sky aerosol DRE is similar to that of the clear-sky, except with secondary influences of the clouds: The cloud radiative effect is strongest (most negative) in the spring, which reduces the all-sky aerosol DRE. The relative uncertainties in all-sky aerosol DRE due to measurement errors are generally comparable to those in clear-sky conditions except for the aerosol single-scattering albedo. The TOA all-sky aerosol DRE relative uncertainty due to aerosol single-scattering albedo uncertainty is larger than that in clear-sky, leading to a larger total relative uncertainty. The measurement errors in cloud properties have small effects on the all-sky aerosol DRE.

1 Introduction

Aerosols modify Earth's radiative energy budget directly via scattering and absorbing radiation, which is referred to as the aerosol direct radiative effect (DRE). The aerosol DRE is also referred to as the radiative effect due to aerosol-radiation interactions (RE_{ari}) in the Intergovernmental Panel on Climate Change (IPCC) report (Boucher et al., 2013). In order to quantify the aerosol DRE, knowledge of aerosol optical properties including aerosol optical depth (AOD), single-scattering albedo, and asymmetry factor, are required vertically and spectrally, along with the characterization of the surface properties, cloud optical properties, atmospheric state, and Sun-Earth geometry.

All-sky global-mean shortwave (SW) aerosol DRE estimates at the top of the atmosphere (TOA) are about -2 W m^{-2} (e.g., Henderson et al., 2013; Matus et al., 2015, 2019; Oikawa et al., 2018). Passive satellite remote sensing estimates of the aerosol DRE rely on column-averaged observations that are often limited to cloud-free ocean (Yu et al., 2006). Active sensors such as the CloudAerosol Lidar and Infrared Pathfinder Satellite (CALIPSO) provides the opportunity to have vertical profiles of aerosol and clouds over both ocean and land, which allows for more comprehensive all-sky aerosol DRE global estimates. However, several studies have documented that optically thinner aerosol can go undetected by CALIPSO (Redemann et al., 2012; Kacenelenbogen et al., 2014; Rogers et al., 2014; Omar et al., 2013; Thorsen & Fu, 2015b). Thorsen and Fu (2015b) showed that CALIPSO does not detect all radiatively significant aerosols due to instrument sensitivity. Thorsen et al. (2017) further showed that the undetected aerosols result in an underestimate of the global mean AOD, which ultimately leads to an underestimate in the global mean aerosol DRE of up to $\sim 50\%$.

Ground-based observations provide the opportunity to make regional estimates of the aerosol DRE (e.g., Bansal et al., 2019; Di Biagio et al., 2009; Che et al., 2019; Di Biagio et al., 2010; Mortier et al., 2016; Sherman & McComiskey, 2018; Xia et al., 2016). Regional estimates can then be useful to compare and validate satellite estimates. The high-quality ground-based observations at the Atmospheric Radiation Measurement Program (ARM) sites (Ackerman & Stokes, 2003) provide the opportunity to utilize obser-

63 vations of aerosol, cloud, radiation, and the atmospheric state to quantify the aerosol DRE.
64 Previous studies have quantified the clear-sky aerosol DRE at the ARM sites (e.g., Fu
65 et al., 1999; Delene & Ogren, 2002; Iziomon & Lohmann, 2003; Michalsky et al., 2006;
66 Creekmore et al., 2014; Wu et al., 2021). However, no study to date has quantified the
67 all-sky aerosol DRE at the ARM sites based on ground-based observations.

68 In Wu et al. (2021), we quantified the clear-sky aerosol DRE at the ARM South-
69 ern Great Plains (SGP) and Tropical Western Pacific (TWP) sites using multi-year ground-
70 based observations. Herein we quantify the all-sky aerosol DRE by considering the aerosol
71 DRE for both cloudy-skies and clear-skies at the ARM SGP site. Note that we do not
72 consider the ARM TWP site in this study as we did in Wu et al. (2021) due to the lim-
73 ited data availability hampering the ability to estimate the cloudy-sky aerosol DRE.

74 By inputting the ground-based observations into the NASA Langley Fu-Liou ra-
75 diative transfer (RT) model (Fu & Liou, 1992, 1993; Fu, 1996; Fu et al., 1998; F. G. Rose
76 & Charlock, 2002; F. Rose et al., 2006), the regional aerosol DRE can be estimated by
77 quantifying how the radiative fluxes change in an atmosphere with and without aerosols.
78 As in Wu et al. (2021), the ground-based Raman lidars (RL) (Ferrare et al., 2006; Gold-
79 smith et al., 1998; Newsom, 2009) are utilized for aerosol vertical detection and extinc-
80 tion profile (Balmes et al., 2019; Balmes & Fu, 2018; Thorsen & Fu, 2015a; Thorsen et
81 al., 2015; Thorsen & Fu, 2015b; Thorsen et al., 2017) while the Aerosol Robotic Network
82 (AERONET) Cimel sun photometers provide aerosol optical depth, single-scattering albedo,
83 and asymmetry factor at several wavelengths (Holben et al., 1998; Giles et al., 2019). To
84 estimate the aerosol DRE under cloudy-skies, the RL cloud vertical detection and ex-
85 tinction profiles are utilized. In addition, the Active Remote Sensing of Clouds (ARSCL)
86 value-added product (Clothiaux et al., 2001) from the Ka-band Zenith ARM radar (KAZR)
87 and the millimeter cloud radar (MMCR) supplements the RL observations to provide
88 cloud and precipitation observations when the lidar becomes fully attenuated. The all-
89 sky aerosol DRE is then quantified in terms of the daily mean, monthly mean, seasonal
90 cycle, and annual-mean climatology.

91 Section 2 describes the aerosol and cloud optical properties from the RL, KAZR,
92 and MMCR, as well as the RT model and other observational data employed in this study.
93 Section 3 presents the radiative closure experiment under cloudy-sky condition by com-
94 paring simulated surface downwelling SW fluxes using observed inputs with correspond-
95 ing observed fluxes. Section 4 presents the daily mean as well as the seasonal cycle of
96 the all-sky aerosol DREs. Section 5 quantifies the measurement uncertainties for the es-
97 timated all-sky aerosol DREs. Section 6 summarizes and presents concluding remarks.

98 2 Data and Radiation Model

99 2.1 Aerosol and cloud profiles

100 2.1.1 ARM RL

101 The ARM Raman lidar (RL) (Ferrare et al., 2006; Goldsmith et al., 1998; New-
102 som, 2009) provides vertical profiles of retrieved aerosol and cloud extinction at 355 nm
103 from the feature detection and extinction (RL-FEX) retrieval algorithm (Balmes et al.,
104 2019; Balmes & Fu, 2018; Thorsen et al., 2015; Thorsen & Fu, 2015a; Thorsen et al., 2017;
105 Wu et al., 2021). In this study, a temporal resolution of 10 minutes and a vertical res-
106 olution of 30 meters are considered from 1 August 2008 to 31 August 2016 at the South-
107 ern Great Plains (SGP) site in Lamont, Oklahoma (36.61°N, 97.49°W). Profiles in which
108 the lidar beam does not fully attenuate are referred to as transparent profiles, which are
109 those when the signal-to-noise ratio (SNR) is greater than 1 at 16 km (Balmes et al., 2019;
110 Thorsen et al., 2015).

111 Figures 1a and 1b show an example of feature classification and extinction coef-
112 ficient from the RL, respectively, as a function of time and height retrieved on 28 Jan-
113 uary 2013 over the ARM SGP site. On this day, there are periods of clear-skies until around
114 12 UTC and then cloudy-skies after that. Ice clouds are present around 10-12 km and
115 liquid clouds are present around 0.5-2.5 km after around 16 UTC. From 12-18 UTC and
116 then again after 21 UTC, the cloudy-sky profiles are transparent to the RL, which we
117 refer to as transparent cloudy-sky. There are a few intervals of cloudy-sky periods dur-
118 ing 18-21 UTC when the RL fully attenuates, which are referred to as opaque cloudy-
119 sky.

120 The occurrence fraction of clear-sky, transparent cloudy-sky, and opaque cloudy-
121 sky for the entire 8-year time period at SGP is presented in Fig. 2. The clear-sky frac-
122 tion is 0.38 and the cloud fraction is 0.62. The cloud fraction is further separated into
123 transparent and opaque cloudy-sky as described above, which correspond to 0.32 and
124 0.30, respectively.

125 In this study, RL aerosol and cloud extinction profiles are used for clear-sky and
126 transparent cloudy-sky profiles. For the aerosol profiles in opaque cloudy-sky conditions,
127 the RL aerosol extinction profile below the level where the RL signal becomes fully at-
128 tenuated is utilized. For the atmosphere above the RL attenuated level, the weekly mean
129 cloudy-sky aerosol extinction profile is used at levels where the radar did not detect clouds
130 or precipitation and cloud liquid and ice water profiles are based on the radar retrievals
131 as described next.

132 In addition to the RL extinction profile for transparent cloudy-sky profiles, the cloud
133 particle size is also needed as input to the radiative transfer model (Section 2.2). The
134 liquid cloud effective radius is set as 6.54 microns for transparent cloudy-sky profiles, which
135 is used in multiple retrieval algorithms (Zhao et al., 2012) as well as in the RL retrieval
136 algorithm (Thorsen & Fu, 2015a). The ice cloud effective diameter is derived as a func-
137 tion of temperature following Heymsfield et al. (2014).

138 *2.1.2 Radar retrievals*

139 For opaque cloudy-sky profiles in which the RL fully attenuated, the Active Re-
140 mote Sensing of Clouds (ARSCL) value-added product (Clothiaux et al., 2001) is used
141 to retrieve cloud properties. ARSCL from the millimeter cloud radar (MMCR) is used
142 for August 2008 - January 2011 and from the Ka-band ARM Zenith Radar (KAZR) for
143 January 2011 - August 2016. The temporal resolution is 10 seconds and the vertical res-
144 olution is 43 meters for the MMCR and 4 seconds and 30 meters for the KAZR. The cloud
145 retrievals are adapted from those used in Thorsen et al. (2013) and the ARM value-added
146 products MICROBASE (Dunn et al., 2011) and CombRet (J. M. Comstock et al., 2013). The
147 cloud layer boundaries, reflectivity, and temperature are used to retrieve cloud water con-
148 tent with the phase determined by temperature following MICROBASE (Dunn et al.,
149 2011).

150 For liquid clouds, the liquid water content (LWC) is retrieved from reflectivity fol-
151 lowing Liao and Sassen (1994) with the cloud particle number concentration set as 100
152 cm^{-3} (Dunn et al., 2011). For opaque cloudy-sky profiles, the liquid cloud effective ra-
153 dius is retrieved from the LWC following Frisch et al. (1995) and Dunn et al. (2011) with
154 the assumption of a log-normal droplet distribution with a width of 0.35. In contrast to
155 Dunn et al. (2011), the cloud particle number concentration is set as 100 cm^{-3} follow-
156 ing Thorsen et al. (2013).

157 For ice clouds, the ice water content (IWC) is retrieved from temperature and re-
158 flectivity following Hogan et al. (2006). In the same manner as transparent cloudy-sky
159 (Section 2.1.1), the opaque cloudy-sky ice cloud effective diameter is from Heymsfield
160 et al. (2014).

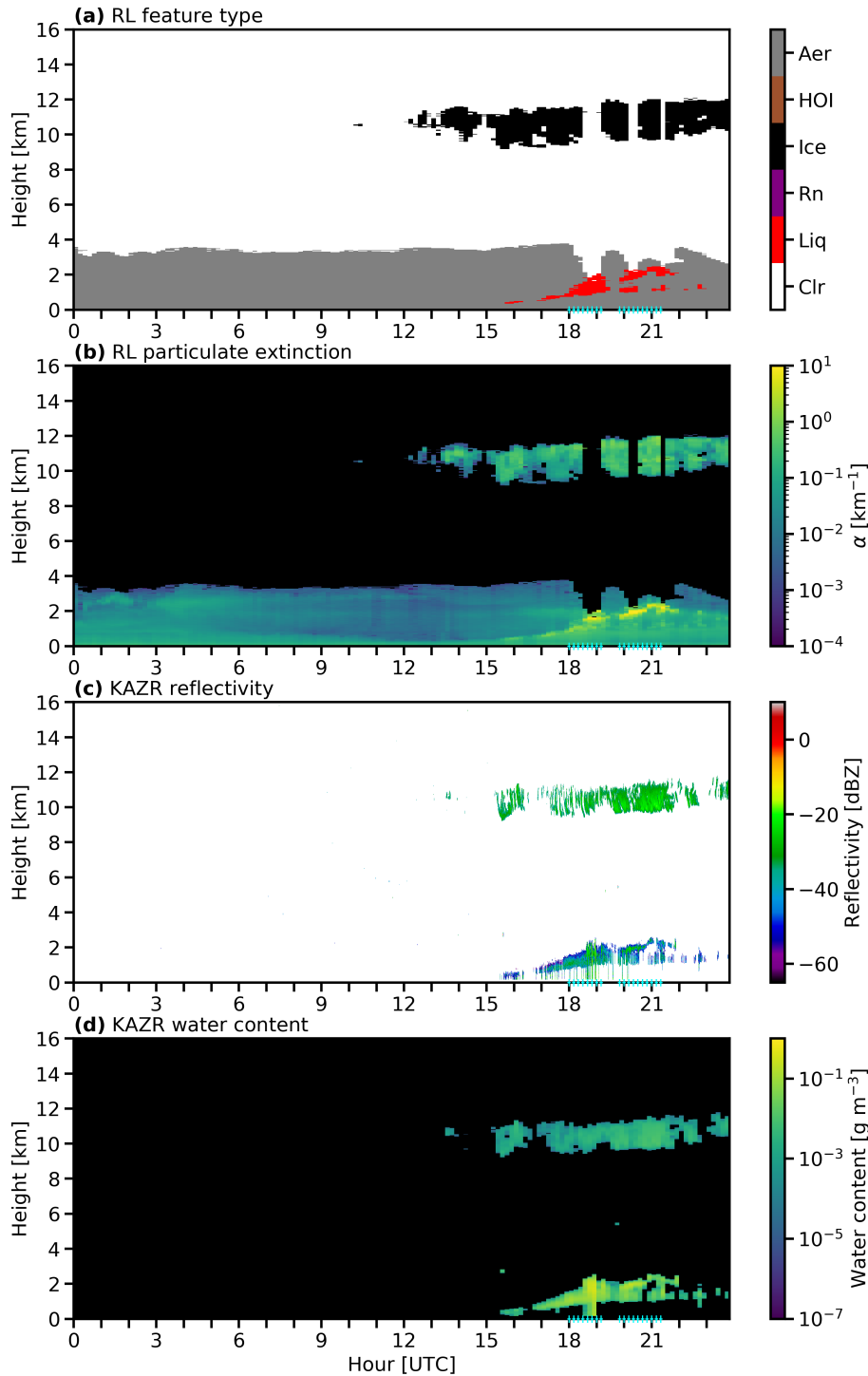


Figure 1. Raman lidar (RL) and Ka-band ARM Zenith Radar (KAZR) observations on 28 January 2013 at the Southern Great Plains (SGP) site. (a) RL feature type as liquid cloud (red), rain (purple), horizontally-oriented ice (HOI; brown), ice cloud (black) or aerosol (grey). (b) RL feature particulate extinction (α ; km^{-1}) at 355 nm. (c) KAZR reflectivity (dBZ). (d) KAZR-retrieved hydrometeor water content (g m^{-3}). The light blue + along the x-axis indicates the periods when the RL became fully attenuated.

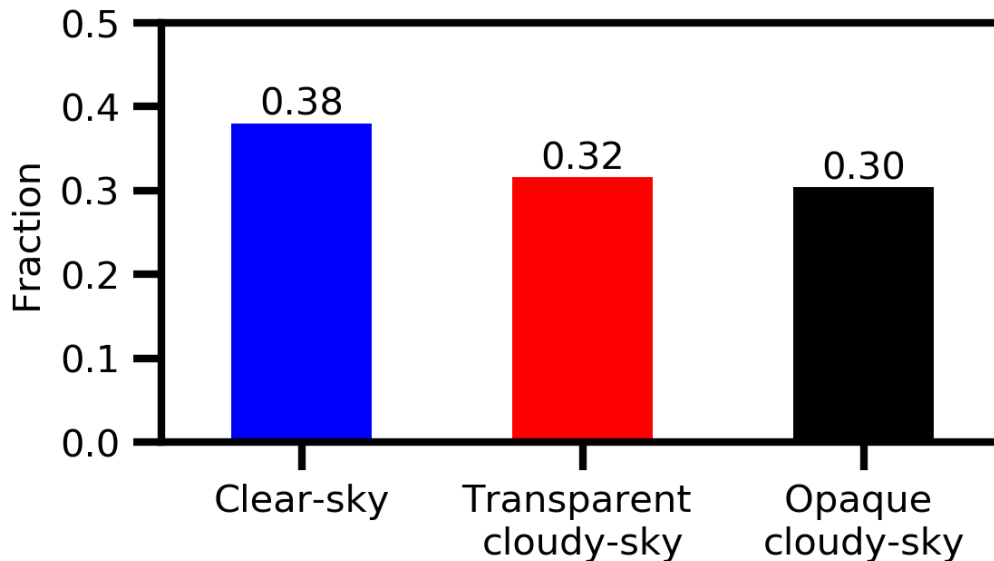


Figure 2. Clear-sky (left) and cloud fractions for the Raman lidar (RL) at the Southern Great Plains (SGP) site from August 2008 to August 2016. The cloud fraction is partitioned into those transparent (middle) and opaque (right) to the RL. The fraction is labeled above each bar.

161 When the reflectivity is greater than -7 dBZ with temperature greater than 0 °C
 162 (Fueglistaler & Fu, 2006), we consider the reflectivity to be due to liquid precipitation.
 163 The rain water content (RWC) is retrieved from the reflectivity following Wood (2005).
 164 After the liquid water content is retrieved, it is run again with the corrected reflectiv-
 165 ity to consider the attenuation by water drops (Lhermitte, 1990). The water content is
 166 then averaged temporally to match the RL temporal resolution of 10 minutes.

167 Figures 1c and 1d show an example of the KAZR reflectivity and KAZR-retrieved
 168 water content, respectively, for 28 January 2013 over SGP. The radar-retrieved water con-
 169 tent profiles are considered during the intervals of opaque cloudy-sky times from 18-21
 170 UTC.

171 When available, the cloud liquid water path (LWP) retrieved from the radar is scaled
 172 to match the LWP from the ground-based microwave radiometer (MWR) (Gaustad et
 173 al., 2011). The temporal resolution of the MWR is 20 seconds and it is averaged to match
 174 the RL temporal resolution of 10 minutes. If MWR observations are unavailable, a fit
 175 between the radar-retrieved LWP and MWR LWP from all collocated observations in
 176 each month is utilized to scale the radar-retrieved LWP. We scale the radar-retrieved cloud
 177 LWC using MWR LWP for liquid clouds since we have much more confidence on the lat-
 178 ter based on the quantified uncertainties (Gaustad et al., 2011). An example of the col-
 179 located radar-retrieved and MWR LWP observations for January 2013 is shown in Fig.
 180 3a where the orthogonal distance regression line is obtained by using 794 pairs of LWP
 181 observations with a coefficient of determination (r^2) of 0.34. The fitting is applied to each
 182 month to find a scaling relationship that is then applied to the opaque cloudy-sky LWC
 183 profile when the MWR is not available.

184 Similar to the LWC scaling, we scale the radar-retrieved cloud IWC using RL cloud
 185 optical depth for ice clouds since again we have more confidence on the RL retrieval based
 186 on associated uncertainty (Thorsen & Fu, 2015a; Balmes et al., 2019). The radar-retrieved
 187 IWC profiles in opaque cloudy-sky conditions are scaled as follows. The scaling relation-

ship is found by using collocated observations of radar-retrieved and RL ice cloud column optical depth when the RL is transparent. The ice cloud column optical depth is further restricted to vertical levels where both instruments detect ice clouds. The effective radius of ice particles as a function of temperature following Heymsfield et al. (2014) is used along with the radar-retrieved IWC profile to obtain its ice cloud optical depth. An example of the collocated radar-retrieved and RL ice cloud column optical depth for January 2013 is shown in Fig. 3b where there are 854 collocated observations and the orthogonal distance regression line has a r^2 of 0.62. A scaling relationship is found for each month and each opaque cloudy-sky IWC profile is then scaled accordingly.

2.2 Radiative transfer model and other data

The radiative transfer model and remaining data utilized in this study, which are the same as those used in Wu et al. (2021), are briefly described below. For further details, see Sections 2 and 3 in Wu et al. (2021).

The aerosol and cloud profiles are inputted into the NASA Langley Fu-Liou radiative transfer model (Fu & Liou, 1992, 1993; Fu, 1996; Fu et al., 1998; F. G. Rose & Charlack, 2002; F. Rose et al., 2006). In this study, we only consider the shortwave (SW) fluxes since the longwave aerosol DRE is orders of magnitude smaller for aerosols common at SGP (e.g., Reddy et al., 2005).

In addition to the RL aerosol extinction profiles, other column-mean aerosol properties come from the Aerosol Robotic Network (AERONET) Version 3 (V3) Level 2 AEROSOL OPTICAL DEPTH and Level 1.5 AEROSOL INVERSIONS datasets for spectral aerosol optical depth (AOD), single-scattering albedo, and asymmetry factor (Giles et al., 2019). The Angstrom exponent is used for the AOD at wavelengths outside the observational spectral range. For the spectral range beyond the observed wavelengths, the single-scattering albedo and asymmetry factor is constructed from a combination of 84% urban and 16% sulfate droplets (based on the aerosol models of D’Almeida et al. (1991) and Hess et al. (1998)), which best matched the AERONET spectral single-scattering albedo observations (Wu et al., 2021).

The MODerate Resolution Imaging Spectroradiometer (MODIS) MCD43C1 Version 6 Bidirectional Reflectance Distribution Function (BRDF) and Albedo Model Parameters dataset (Schaaf et al., 2002; Roesch et al., 2004) is utilized for the surface albedos. Atmospheric state profiles are from radiosondes for temperature and water vapor, and from the European Centre for Medium-Range Weather Forecasts (ECMWF) reanalysis product, ERA-Interim (Dee et al., 2011) for ozone. National Oceanic and Atmospheric Administration (NOAA) Earth System Research Laboratory (ESRL) observations of trace gas concentrations of CO_2 , N_2O , CH_4 , and CFCs are also used.

Surface SW flux observations are from the ARM QCRAD data product (Long & Shi, 2006, 2008). The downwelling surface SW fluxes considered are the direct (F_{direct}^\downarrow), diffuse ($F_{diffuse}^\downarrow$), and the sum of the direct and diffuse, or the total (F_{total}^\downarrow) at the horizontal surface. The simulated downwelling surface SW fluxes are compared with observed downwelling surface SW fluxes for cloudy-sky conditions through a radiative closure experiment in the next section.

3 Radiative Closure Experiment

Simulated surface SW broadband radiative fluxes based on cloudy-sky observed inputs are compared with radiometer observations to evaluate the radiative transfer model with the observed input, which is commonly referred to as a radiative closure experiment (e.g., Mace et al., 2006; Michalsky et al., 2006; Mather et al., 2007; Miller & Slingo, 2007; J. M. Comstock et al., 2013; Shupe et al., 2015; McComiskey & Ferrare, 2016). Radia-

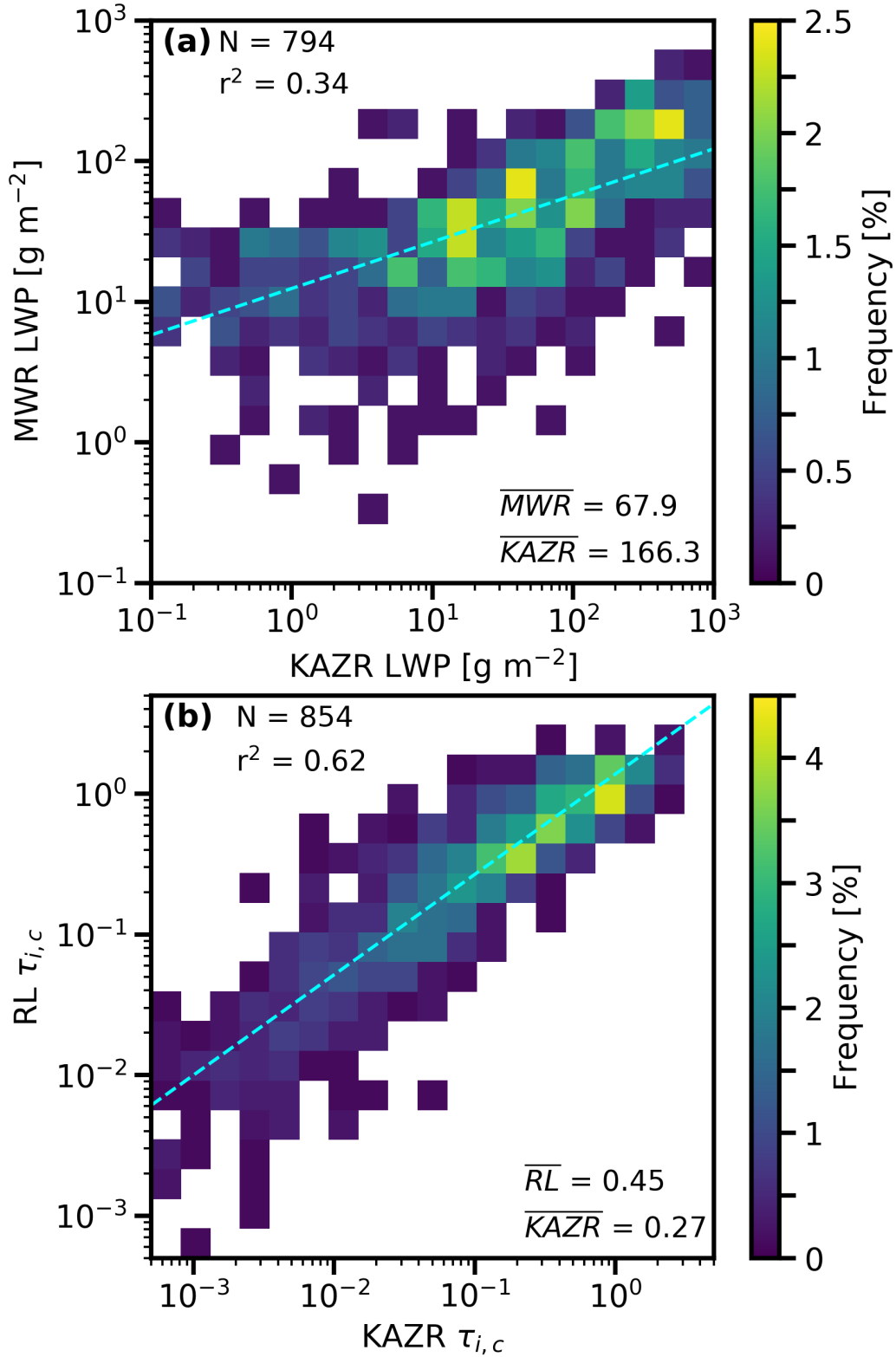


Figure 3. Frequency histogram of collocated (a) Ka-band ARM radar (KAZR) and microwave radiometer (MWR) cloud liquid water path (LWP) and (b) KAZR and Raman lidar (RL) ice cloud column optical depth for January 2013. The regression lines are shown as dashed light blue lines. The sample size (N) and coefficient of determination (r^2) are given in the top left of each plot. The mean value of KAZR (\overline{KAZR}), MWR (\overline{MWR}), and RL (\overline{RL}) observations are shown in the bottom right.

236 tive closure experiments typically focus on clear-sky observations and only limited case
 237 studies have been done at the SGP site for cloudy-skies for SW downwelling fluxes (e.g.,
 238 Lane et al., 2002; Min et al., 2003; Turner et al., 2007).

239 In Wu et al. (2021) we compared simulated and observed surface SW fluxes for clear-
 240 skies at SGP and found excellent agreement with a mean difference of 1 W m^{-2} in F_{total}^{\downarrow} .
 241 In this study, we investigate the cloudy-sky radiative closure by considering transpar-
 242 ent cloudy-sky profiles and opaque cloudy-sky profiles separately. For the opaque cloudy-
 243 sky profiles, we consider cases with collocated RL, radar, and MWR observations. The
 244 radiative transfer model inputs (e. g., aerosol and cloud optical properties, surface albedo,
 245 atmospheric state) are detailed in Section 2.

246 To limit the impact of cloud horizontal inhomogeneity that cannot be observed by
 247 the zenith-view of the RL and radar for given time, we only consider cases when the ob-
 248 served F_{direct}^{\downarrow} is greater (less) than 10 W m^{-2} for the transparent (opaque) cloudy-sky
 249 situation, and the cosine of the solar zenith angle is greater than 0.15. Figure 4 compares
 250 the simulated and observed fluxes for the transparent cloudy-sky (Fig. 4a) and opaque
 251 cloudy-sky (Fig. 4b) profiles.

252 For the transparent cloudy-skies, the mean (relative) differences in F_{total}^{\downarrow} , F_{direct}^{\downarrow} ,
 253 and $F_{diffuse}^{\downarrow}$ are 31.85 (6.0%), 37.71 (10.8%), and -5.87 (-3.3%) W m^{-2} , respectively.
 254 The correlation coefficients between simulated and observed fluxes for F_{total}^{\downarrow} , F_{direct}^{\downarrow} , and
 255 $F_{diffuse}^{\downarrow}$ are 0.76, 0.66, and 0.83, respectively. The overestimation of simulated F_{direct}^{\downarrow}
 256 indicates that the cloud optical depth in the direction of the solar direct beam is gen-
 257 erally larger than the RL-derived cloud optical depth divided by the cosine of the solar
 258 zenith angle, which might be largely caused by the cloud horizontal inhomogeneity. The
 259 exponential relationship between the optical depth and F_{direct}^{\downarrow} could potentially result
 260 in the 10-minute averaged observed flux to exceed the 10-minute modeled flux (based
 261 on the average optical depth). However, the opposite bias is seen as there is a positive
 262 bias in the simulated F_{direct}^{\downarrow} , which suggest that any non-linearity effects are compen-
 263 sated by another dominant factor.

264 For the opaque cloudy-skies, the mean differences in F_{total}^{\downarrow} and $F_{diffuse}^{\downarrow}$ are -13.23
 265 and -11.85 W m^{-2} , respectively, corresponding to relative differences of $\sim -7.2\%$ and $-$
 266 6.5% . The correlation coefficients between modeled fluxes and observations are 0.86 for
 267 both F_{total}^{\downarrow} and $F_{diffuse}^{\downarrow}$.

268 The sensitivity of the results to the solar zenith angle is assessed by considering
 269 stricter solar zenith angle thresholds (e.g., $\cos(\text{SZA}) > 0.3$). For increasing $\cos(\text{SZA})$,
 270 the transparent cloudy-sky results switch from a positive bias in F_{total}^{\downarrow} and F_{direct}^{\downarrow} to a
 271 negative bias while the $F_{diffuse}^{\downarrow}$ negative bias increases. For example, the relative dif-
 272 ferences in F_{total}^{\downarrow} , F_{direct}^{\downarrow} , and $F_{diffuse}^{\downarrow}$ are $\sim -6.7\%$, -6.8% , and -6.5% when considering
 273 only profiles when $\cos(\text{SZA}) > 0.8$. The opaque cloudy-sky radiative closure results were
 274 largely invariant of the solar zenith angle threshold and the mean difference in F_{total}^{\downarrow} was
 275 $\sim -13 \text{ W m}^{-2}$ and $F_{diffuse}^{\downarrow}$ was $\sim -12 \text{ W m}^{-2}$ for nearly all solar zenith angle thresholds
 276 considered.

277 The sensitivity of the results to the observed F_{direct}^{\downarrow} threshold (10 W m^{-2}) is ex-
 278 amined by considering all transparent and opaque cloudy-sky profiles. For transparent
 279 cloudy-sky profiles, the mean differences in F_{total}^{\downarrow} , F_{direct}^{\downarrow} , and $F_{diffuse}^{\downarrow}$ are 34.36, 38.49,
 280 and -4.13 W m^{-2} , respectively, corresponding to relative differences of $\sim 6.7\%$, 11.4% ,
 281 and -2.3% . For the opaque cloudy-skies, the mean differences in F_{total}^{\downarrow} and $F_{diffuse}^{\downarrow}$ are
 282 -43.50 and -9.37 W m^{-2} , respectively, corresponding to relative differences of $\sim -16.6\%$
 283 and -4.1% . While the results indicate a worse agreement in F_{total}^{\downarrow} for the opaque cloudy-
 284 sky, the results are similar overall and even better in $F_{diffuse}^{\downarrow}$.

Overall, the agreement is good as the mean difference is smaller than about 10% with large correlation coefficients. While the mean differences were significantly smaller for clear-sky conditions (Wu et al., 2021), some disagreement for cloudy-sky conditions is expected since the cloud fields are horizontally heterogeneous and therefore difficult to capture with zenith-pointing instruments. In addition, the 3D effects of radiative transfer are not captured by using a 1D radiative transfer model (e.g., Fu et al., 2000).

Another reason for the disagreement could be related to errors in retrieved cloud optical depth. By decreasing the opaque cloudy-sky cloud optical depth by 10%, the mean difference between the observed and simulated fluxes becomes less than 2 W m^{-2} for F_{total}^{\downarrow} and less than 1 W m^{-2} $F_{diffuse}^{\downarrow}$. For the transparent cloudy-sky situation, however, an increase or decrease in cloud optical depth only leads to a small change in the F_{total}^{\downarrow} since the changes in the F_{direct}^{\downarrow} and $F_{diffuse}^{\downarrow}$ are opposite in sign and largely cancel each other. For example, when the transparent cloudy-sky cloud optical depth is increased by 10%, the mean (relative) differences in F_{total}^{\downarrow} , F_{direct}^{\downarrow} , and $F_{diffuse}^{\downarrow}$ are 30.08 (5.7%), 31.79 (9.1%), and -1.71 (-0.9%) W m^{-2} , respectively. This suggests that the mean differences between observed and simulated fluxes for the transparent cloudy-sky are likely related to the cloud inhomogeneity and 3D effects. It is also worth noting that we have confidence on the transparent cloudy-sky cloud optical depth in the zenith direction based on RL observations. It will be shown later (Table 1) that the aerosol DRE is less sensitive to changes in cloud microphysical and optical properties. For example, a 10% change in the transparent cloud optical depth results in a less than 1% change in the aerosol DRE (the impact of a 10% change in the opaque cloud optical depth is even smaller).

4 All-sky aerosol direct radiative effect

The instantaneous aerosol DRE is defined as:

$$DRE = [F^{\downarrow} - F^{\uparrow}]_{aerosol} - [F^{\downarrow} - F^{\uparrow}]_{no \text{ aerosol}}, \quad (1)$$

where F^{\downarrow} is the downward flux and F^{\uparrow} is the upward flux. Equation 1 is evaluated considering fluxes at the top of the atmosphere (TOA) for the TOA aerosol DRE and at the surface (SFC) for the SFC aerosol DRE. The aerosol DRE is calculated by running the radiative transfer model with and without aerosols for the same atmospheric profile. The aerosol DRE is considered across three time scales in this study, including the (1) daily, (2) monthly, and (3) annual mean aerosol DREs.

The daily mean aerosol DRE, \overline{DRE} , is calculated as:

$$\overline{DRE} = \frac{1}{24 \text{ hr}} \int_{sunrise}^{sunset} DRE(t) dt, \quad (2)$$

where $DRE(t)$ is the instantaneous aerosol DRE at given time t . The solar zenith angle effects on the daily mean aerosol DRE are characterized by considering a time step of 30 minutes (Yu et al., 2004, 2006; Balmes & Fu, 2020). Note that the instantaneous aerosol DREs (e.g., Oyola et al., 2019) can be much larger than the daily mean aerosol DREs presented in this study.

4.1 Daily- and monthly-mean time series of all-sky aerosol DREs

The daily mean all-sky aerosol DRE is calculated by considering the instantaneous aerosol DRE at every 30-minute time step. We consider the closest RL observation in

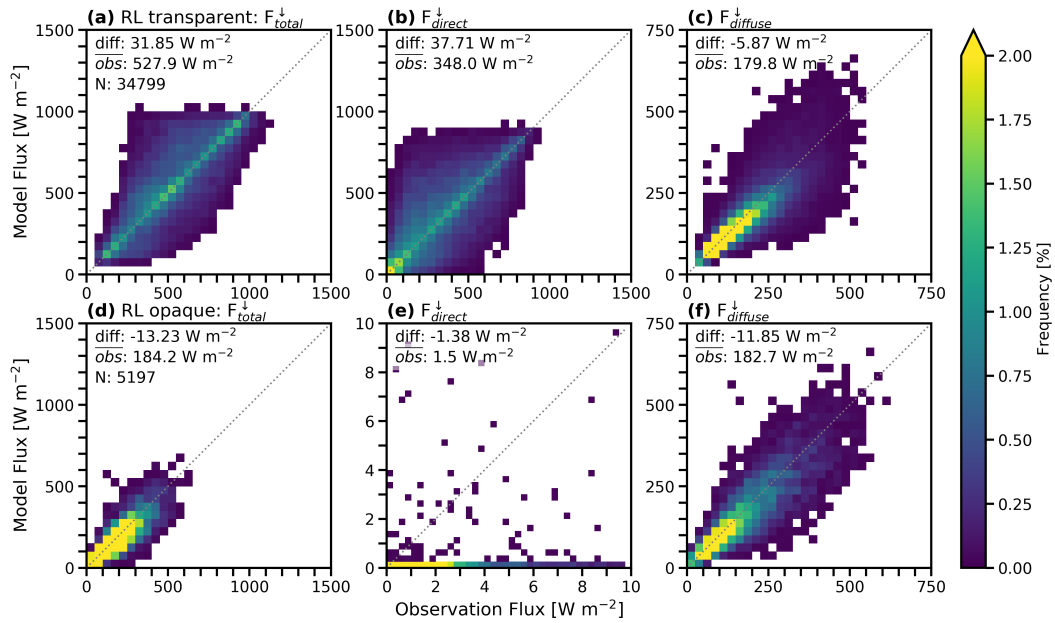


Figure 4. Downwelling surface shortwave (SW) fluxes from the model and observations. The fluxes shown include (a, d) the total downwelling surface SW fluxes, F_{total}^{\downarrow} , (b, e) the direct downwelling surface SW fluxes, F_{direct}^{\downarrow} , and (c, f) the diffuse downwelling surface SW fluxes, $F_{diffuse}^{\downarrow}$. Results are for Raman lidar (RL) transparent cloudy-sky profiles (top) and opaque cloudy-sky profiles (bottom) from August 2008 to August 2016. The 1:1 lines are shown as dashed grey lines. The mean difference (diff) between modeled and observed fluxes and the mean value of the observed fluxes (\overline{obs}) are given in the top left of each plot. The sample size (N) is given in the top left of each plot in the left column.

330 time. When the closest RL observation is clear-sky or transparent cloudy-sky, the RL
331 aerosol and cloud extinction profile is used. When the closest RL observation is opaque
332 cloudy-sky, the closest radar cloud and rain water content profiles are used (Section 2.1.2).
333 The AODs used in the aerosol DRE calculations are scaled so that the (1) monthly mean
334 AOD matches the monthly mean observed AOD (Wu et al., 2021), and that the (2) monthly
335 mean clear-sky RL AOD matches the monthly mean AERONET AOD. The closest AERONET
336 observations of spectral AOD, single-scattering albedo, and asymmetry factor are used
337 if they are available within one week. If no AERONET observation is available within
338 one week, monthly mean AERONET observations are inputted.

339 If the closest RL observation is beyond 1 hour, we do not calculate the instantane-
340 ous aerosol DRE for that 30-minute time step. In addition, if the closest radar obser-
341 vation is beyond 1 hour of the opaque cloudy-sky observation, the instantaneous aerosol
342 DRE is not calculated. The daily mean all-sky aerosol DRE is not estimated for days
343 in which any 30-minute time step does not have an instantaneous aerosol DRE estimate.
344 This results in 2030 days with a daily mean all-sky aerosol DRE estimate out of the 2953
345 days from August 2008 to August 2016. Monthly mean aerosol DREs are constructed
346 by taking the mean of all daily mean estimates in each month.

347 The 2030 days with daily mean aerosol DRE estimates corresponds to 51915 time
348 steps of daylight when considering 30-minute resolution. 91% of the time steps are within
349 the RL profile time interval (i.e., 10 minutes). When they are not, the average time dif-
350 ference between the RL profile central time and the 30-minute time step is 7.7 minutes.
351 Of the time steps that are opaque cloudy-sky, 98% of radar profile times are the same
352 time as the RL profile time. 70% of the opaque cloudy-sky time steps have MWR ob-
353 servations within 1 hour, and 39% are within the MWR time interval. 93% of the time
354 steps have AERONET AOD observations within 1 week and 89% of the time steps have
355 AERONET single-scattering albedo and asymmetry factor observations within 1 week.

356 Figure 5 shows the daily mean all-sky aerosol DRE time series at both the TOA
357 and the surface. The daily mean aerosol TOA DRE at SGP is typically negative with
358 the largest in magnitude negative DRE of -13.42 W m^{-2} . In 259 days (12.8%) of the to-
359 tal 2030 days, the daily mean aerosol DRE is positive with a largest in magnitude pos-
360 itive DRE of 11.38 W m^{-2} . The daily mean aerosol DRE at the surface is always neg-
361 ative with a maximum that is nearly neutral (-0.05 W m^{-2}) to a minimum of -34.87 W
362 m^{-2} . Figure 5 also shows the monthly mean aerosol DRE time series. The monthly mean
363 aerosol DRE varied from 2.24 to -5.83 W m^{-2} at the TOA and from -1.27 to -13.75 W
364 m^{-2} at the surface. Two months have a positive monthly mean aerosol DRE at the TOA
365 (September 2010 and October 2013), while all other 89 monthly mean aerosol DREs are
366 negative. In contrast to the clear-sky aerosol DRE, the all-sky aerosol DRE is typically
367 less negative due to the increased albedo by the clouds, which tends to weaken the aerosol
368 DRE. Consider the clear-sky aerosol DRE in the same 2030 days at SGP for a compar-
369 ison: the TOA daily mean aerosol DRE is positive only for 27 days (1.3%) with a max-
370 imum value of 2.04 W m^{-2} . In addition, the TOA monthly mean aerosol DRE ranges
371 from -0.60 to -7.19 W m^{-2} . Similar to the clear-sky aerosol DRE, the all-sky aerosol DRE
372 is generally stronger (i.e., more negative) during the summer and weaker (i.e., less neg-
373 ative) during the winter. This is related to the seasonal cycle of AOD and daytime frac-
374 tion, which are both larger in the summertime. The all-sky aerosol DRE seasonal cy-
375 cle is investigated in more detail in the next section.

376 4.2 Seasonal cycle and annual mean all-sky aerosol DRE

377 The seasonal cycle of the all-sky aerosol DRE is examined by constructing its monthly
378 mean climatology, which is the mean of all monthly mean estimates for each month. The
379 annual mean climatology of the aerosol DRE is then the mean of the monthly mean cli-
380 matology. Since the daily mean aerosol DRE is not estimated for all 2953 days of the

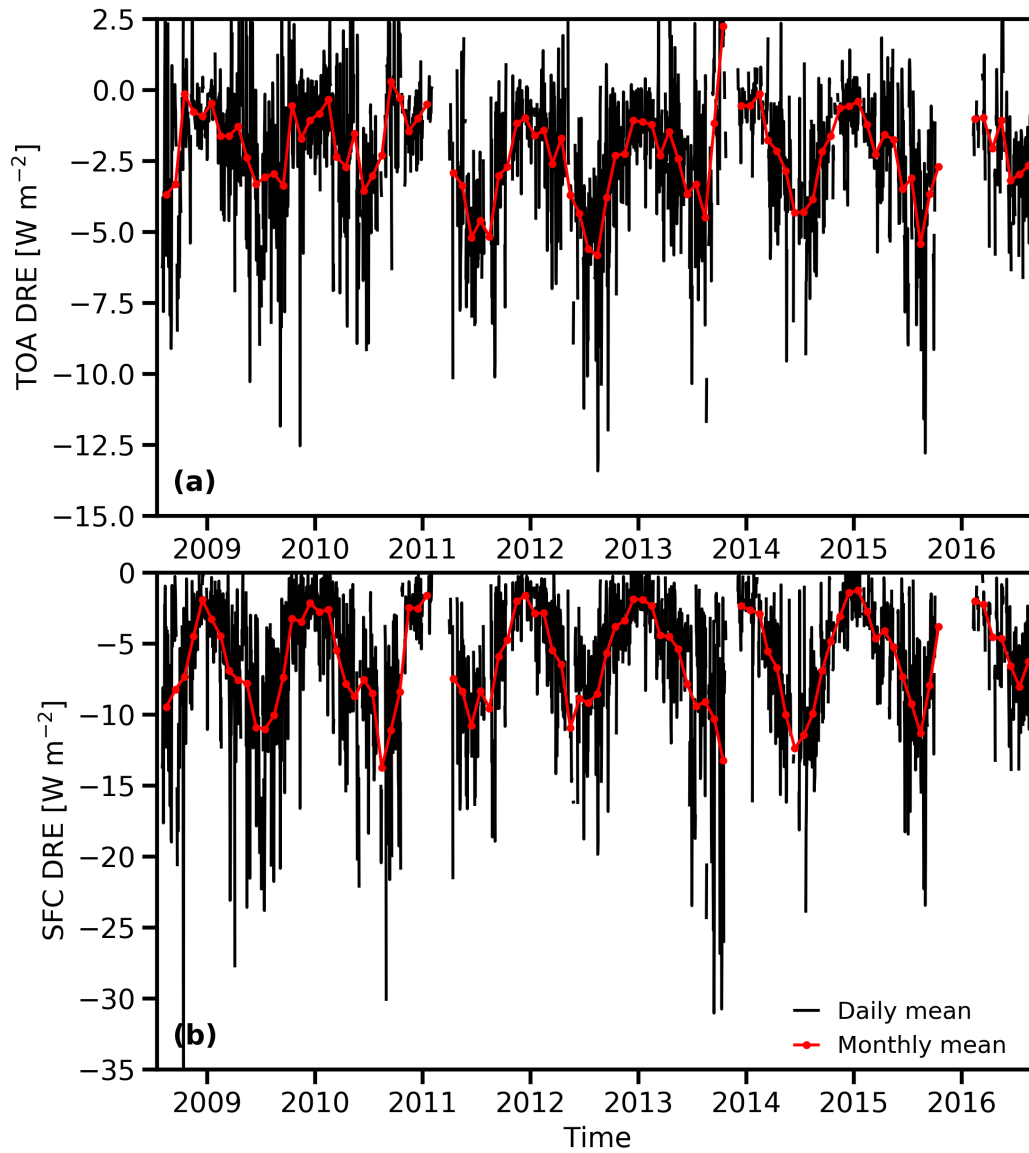


Figure 5. The daily mean (black) and monthly mean (red) all-sky aerosol direct radiative effect (DRE) time series at the Southern Great Plains (SGP) site from August 2008 to August 2016. Results are shown for (a) the top of the atmosphere (TOA) and (b) surface (SFC).

381 8-year study period, its impact on the annual mean aerosol DRE is assessed. The clear-
382 sky annual mean aerosol DRE in Wu et al. (2021) is calculated using all 2953 days, which
383 differed from that by considering the 2030 days by only 0.02 W m^{-2} at both the TOA
384 and surface. This provides confidence that the all-sky aerosol DRE result presented here
385 is capturing the annual mean aerosol DRE despite missing days due to unavailable ob-
386 servations.

387 Figure 6 shows the seasonal cycle of the all-sky aerosol DRE, which largely follows
388 the seasonal cycle of the clear-sky aerosol DRE in Wu et al. (2021) (also shown in Fig.
389 6 for a comparison) with secondary effects from clouds. The strongest aerosol DREs of
390 -3.90 W m^{-2} at the TOA and -9.41 W m^{-2} at the surface are during the summer (June-
391 August) when the AOD is largest. The weakest aerosol DREs correspond to October-
392 February with -1.01 W m^{-2} at the TOA and -3.31 W m^{-2} at the surface.

393 The annual mean all-sky aerosol DRE climatology is -2.13 and -5.95 W m^{-2} at the
394 TOA and surface, respectively. In comparison to the annual mean clear-sky aerosol DRE,
395 the all-sky aerosol DRE is weaker by 0.86 (0.90) W m^{-2} or by 28.8% (13.1%) at the TOA
396 (surface). This is what we expect since the clouds overall weaken the aerosol DRE. The
397 relative difference is comparable to other studies that provide both a clear-sky and all-
398 sky aerosol DRE estimate (e.g., Matus et al., 2015). The annual mean aerosol DRE shows
399 interannual variability (Fig. 5), which for the all-sky (clear-sky) conditions ranges from
400 -1.60 W m^{-2} in 2010 (-2.52 W m^{-2} in 2010) to -3.02 W m^{-2} in 2012 (-3.79 W m^{-2} in
401 2012) at the TOA and from -5.24 W m^{-2} in 2015 (-6.24 W m^{-2} in 2011) to -6.82 W m^{-2}
402 in 2010 (-7.55 W m^{-2} in 2009) at the surface.

403 The all-sky aerosol DRE can be separated into the contribution from clear-sky, trans-
404 parent cloudy-sky, and opaque cloudy-sky. For the annual mean climatology at the TOA
405 (surface), the contributions are -1.15 (-2.89) W m^{-2} from clear-skies, -1.04 (-2.45) W m^{-2}
406 from transparent cloudy-skies, and 0.06 (-0.61) W m^{-2} for opaque cloudy-skies. About
407 50% contribution each from clear-sky and transparent cloudy-sky varies little from month
408 to month (not shown). The transparent cloudy-sky contribution that is nearly the same
409 as that from clear-sky is a result of cancellation effects in the transparent cloudy-sky. The
410 transparent cloudy-sky AOD is larger than the clear-sky AOD (Balmes et al., 2021), which
411 strengthens the aerosol DRE. However, the weakening in aerosol DRE due to cloud re-
412 flection overall compensates the strengthening due to larger AOD. The opaque cloudy-
413 sky contribution is very small and the monthly mean climatology contribution ranges
414 from -0.11 in July to 0.26 W m^{-2} in May, with most months less than 0.10 W m^{-2} in
415 magnitude.

416 The all-sky aerosol DRE estimates in this study provide an estimate with all in-
417 put quantities from observations for a point-location. This can provide a benchmark to
418 compare with satellite and modeling estimates. We compare our all-sky estimates to those
419 from Matus et al. (2019), which estimate the aerosol DRE globally from A-Train satel-
420 lite observations of clouds and aerosols on a 2.5 by 2.5° latitude-longitude grid. For the
421 grid point covering SGP (35 to 37.5°N , 95 to 97.5°W), their all-sky aerosol TOA DRE
422 estimate is -1.86 W m^{-2} annually. Seasonally, their all-sky aerosol TOA DRE estimate
423 is -0.63 W m^{-2} for December-February, -2.13 W m^{-2} for March-May, -1.48 W m^{-2} for
424 June-August, and -2.85 W m^{-2} for September-November. For a comparison, the TOA
425 estimates presented in this study (Fig. 6) are -2.13 W m^{-2} annually, -0.89 W m^{-2} for
426 December-February, -2.12 W m^{-2} for March-May, -3.90 W m^{-2} for June-August, and
427 -1.63 W m^{-2} for September-November. The all-sky aerosol DRE based on satellite ob-
428 servations over the SGP site is 38% of that from the present study in the summer but
429 is 1.75 times of that from the present study in the fall. The latter is a surprise since CALIPSO
430 does not detect all radiatively significant aerosols and underestimated aerosol DREs were
431 expected (e.g., Thorsen & Fu, 2015b; Thorsen et al., 2017). Further research efforts are
432 required to understand such discrepancy between the satellite- and ground-based esti-
433 mates of the aerosol DREs.

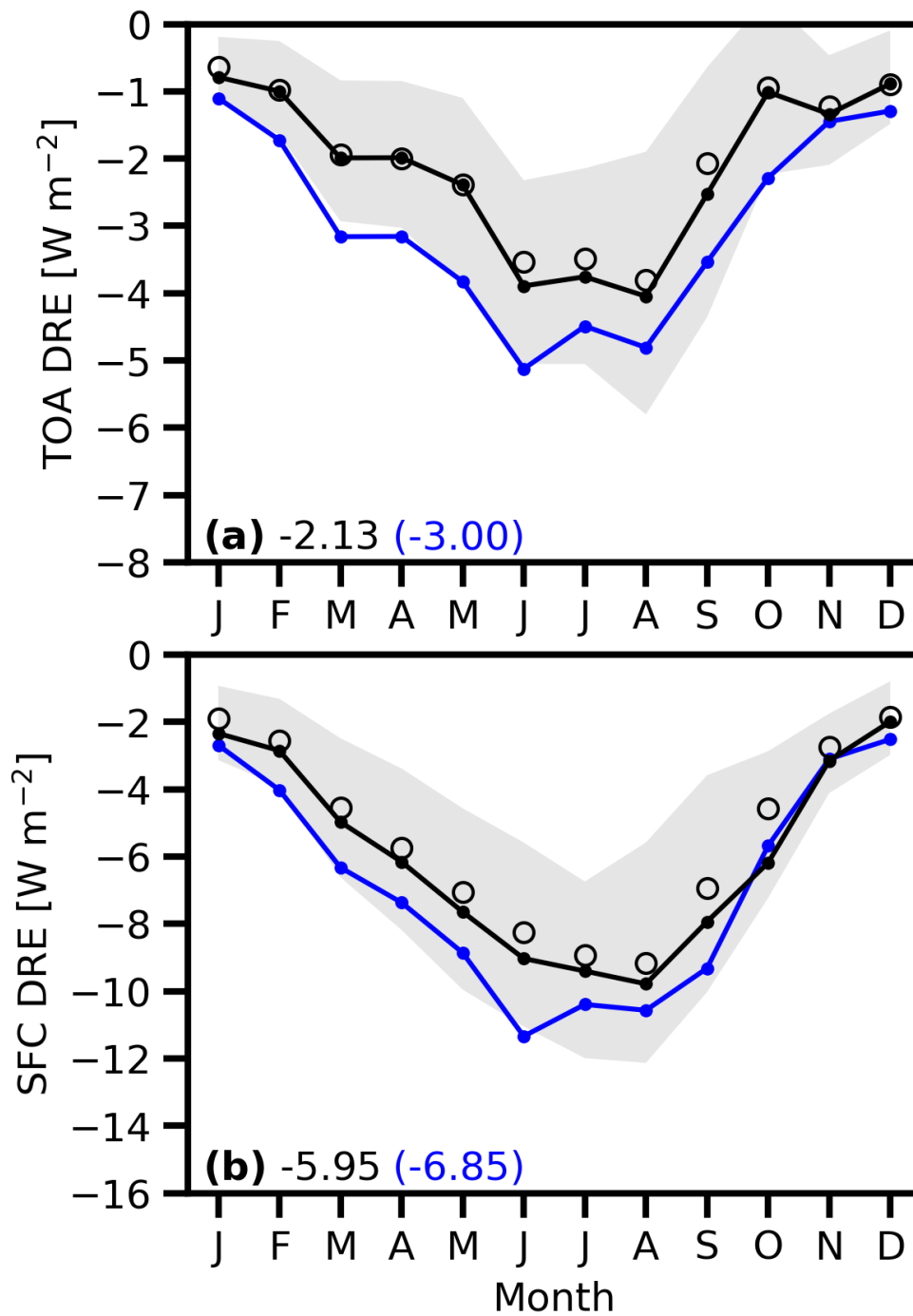


Figure 6. Seasonal cycle of aerosol direct radiative effect (DRE) at the Southern Great Plains (SGP) site from August 2008 to August 2016. Results are shown for (a) the top of the atmosphere (TOA) and (b) the surface (SFC). The aerosol DRE mean (black dots), median (black open circles), and 25th-75th percentile of daily means (shading) are shown. The annual mean climatology values are given in the bottom left. The clear-sky monthly mean climatology is shown in blue along with the annual mean climatology value given in the parentheses for a comparison.

434 To further interpret the differences between the clear-sky and all-sky aerosol DREs
 435 due to clouds, we examine the SW cloud radiative effect (CRE). The daily mean and sea-
 436 sonal cycle CRE are calculated in the same way as the aerosol DRE, except the differ-
 437 ence in fluxes is found by running the radiative transfer model with and without clouds.
 438 The seasonal cycle of the all-sky SW CRE is shown in Fig. 7. The strongest all-sky SW
 439 CRE of -60.54 (-64.69) W m^{-2} occurs in May at the TOA (surface). The stronger CRE
 440 in the springtime (March-May) corresponds to a stronger relative weakening of the all-
 441 sky aerosol TOA DRE compared to clear-sky aerosol TOA DRE ($\sim 37\%$). The weakest
 442 all-sky SW CRE of -16.87 (-17.54) W m^{-2} occurs in November at the TOA (surface),
 443 which corresponds to a small relative weakening of the all-sky aerosol TOA DRE of $\sim 8\%$.

444 Other studies have quantified the CRE at SGP and results are comparable to those
 445 presented here. For example, Mace and Benson (2008) showed the CRE is more nega-
 446 tive in the spring and less negative in the summer and fall and monthly mean climatol-
 447 ogy values range between ~ -20 to -60 W m^{-2} at the TOA and the surface. Dong et al.
 448 (2006) also showed a similar surface all-sky CRE.

449 Figure 8 shows the monthly climatology of all-sky aerosol radiative heating pro-
 450 files (a) and its difference from that under clear-sky conditions (b). The aerosol heat-
 451 ing profile is calculated analogously to the aerosol DRE, but instead considering the dif-
 452 ference in the radiative heating rate profile with and without aerosols. The all-sky heat-
 453 ing profile is similar to the clear-sky heating profile in Wu et al. (2021), which is predom-
 454 inantly near the surface and extends higher into the atmosphere from April to October.
 455 The all-sky heating profile is smaller than the clear-sky heating rates by ~ 0.07 K/day
 456 near the surface and is also slighter smaller between ~ 0.3 and 1.5 km (Fig. 8b) (with
 457 the exception in October). The reduced radiative heating rate in the lower atmosphere
 458 and near the surface is due to clouds reflecting downwelling SW radiation, which over-
 459 all reduces the downwelling solar radiation there. The heating is slightly stronger than
 460 the clear-sky heating rates around $2-3$ km due to aerosol heating above clouds that re-
 461 flect downwelling SW radiation and thus increase the absorption of the SW radiation by
 462 aerosols above. In October, the all-sky radiative heating is larger than the clear-sky heat-
 463 ing including the near surface and lower atmosphere where the impact of the larger aerosol
 464 extinction in cloudy-sky might outweigh the cloud albedo effects.

465 *4.2.1 Sensitivity of annual mean all-sky aerosol DRE to the methods* 466 *used*

467 The sensitivity of annual mean all-sky aerosol DRE to the methods used is exam-
 468 ined. Considering RL observations within 10 minutes instead of 1 hour of each time step
 469 results in a difference of -0.04 W m^{-2} in the annual mean DRE at both the TOA and
 470 surface. The small aerosol DRE difference is largely caused by the reduction of days with
 471 aerosol DRE estimates, which becomes 1798 days.

472 When the radar profile must be within 10 minutes instead of 1 hour, the annual
 473 mean aerosol DRE differed by -0.03 W m^{-2} at both the TOA and surface and the num-
 474 ber of days with aerosol DRE estimates is reduced to 1956 days. MWR observations re-
 475 stricted to within 10 minutes results in an annual mean aerosol DRE difference less than
 476 0.5% . The sensitivity of the aerosol DRE to AERONET observations within 1 week is
 477 assessed by considering observations within 1 day and the difference in aerosol DRE is
 478 found to be within 2% . Overall, the aerosol DRE annual mean estimate is largely insen-
 479 sitive to using observations within 1 hour (or 1 week for AERONET) since the vast ma-
 480 jority of observations are at the same time of the 30-minute time steps considered or closer
 481 than the threshold considered.

482 The sensitivity of the aerosol DRE to the radar-retrieved water content profiles for
 483 the opaque cloudy-sky profiles are tested by using different retrievals. The radar-retrieved
 484 water content is instead retrieved following Frisch et al. (1995) for LWC, Liu and Illing-

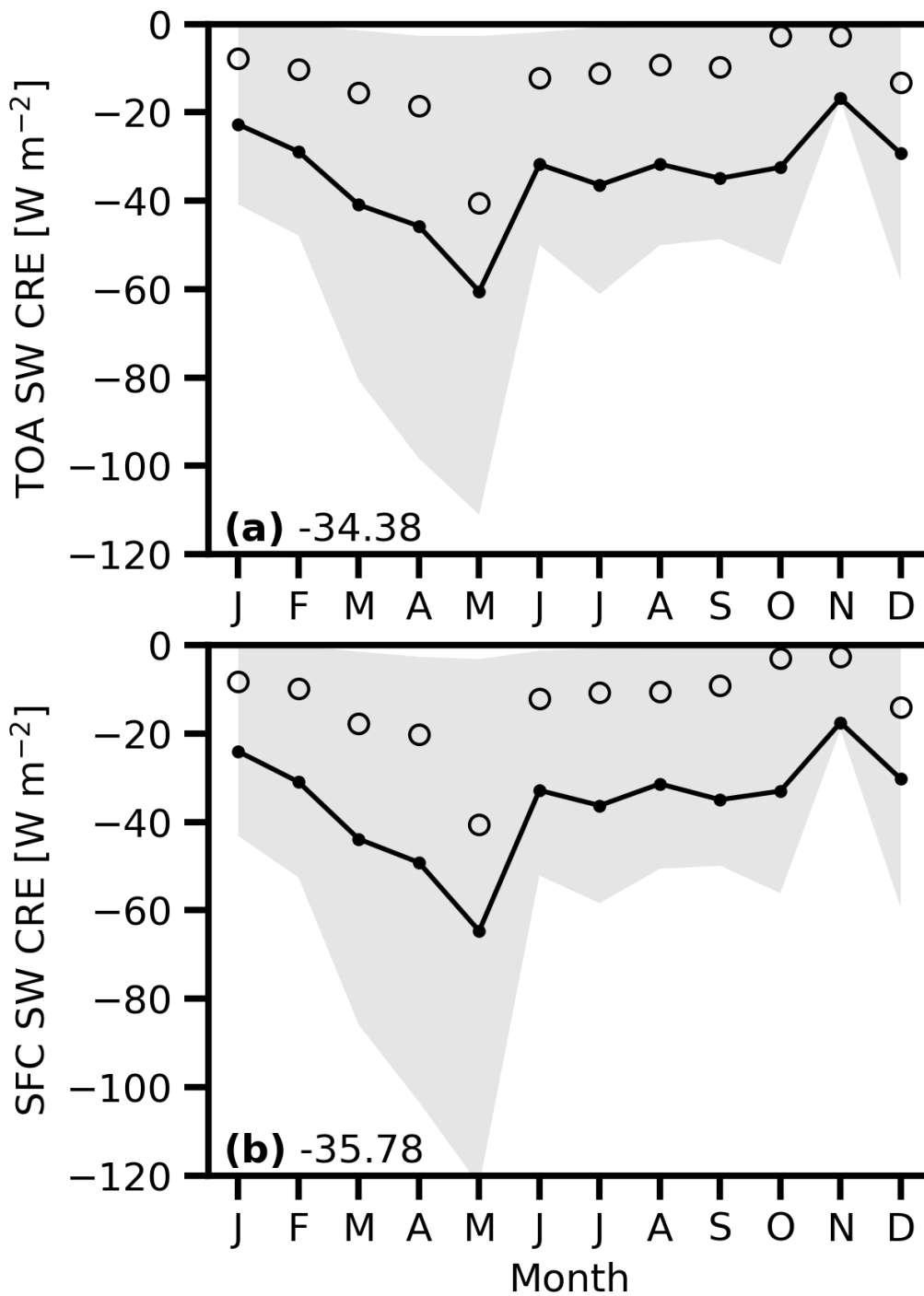


Figure 7. Seasonal cycle of the shortwave (SW) cloud radiative effect (CRE) at the Southern Great Plains (SGP) site from August 2008 to August 2016. Results are shown for the (a) top of the atmosphere (TOA) and (b) surface (SFC). The SW CRE mean (dots), median (open circles), and 25th-75th percentile (shading) are shown. The annual mean climatology values are given in the bottom left.

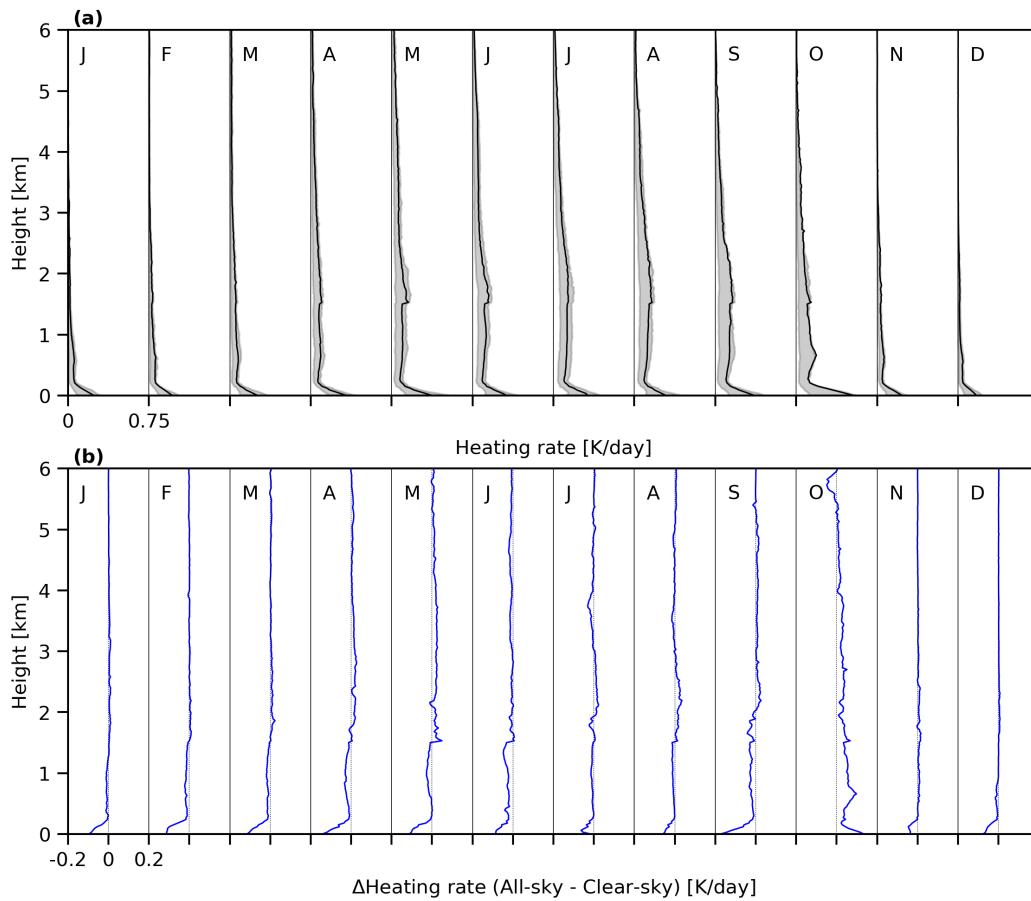


Figure 8. (a) The all-sky aerosol radiative heating rate profile monthly climatology at the Southern Great Plains (SGP) site from August 2008 to August 2016 with the 25th-75th percentile (shading). (b) The difference between the all-sky and clear-sky monthly climatology heating rate profiles (blue line).

485 worth (2000) for IWC, and K. K. Comstock et al. (2004) for RWC. In all cases, the aerosol
 486 DRE differed by less than 0.01 W m^{-2} at both the TOA and surface. This small differ-
 487 ence is because the LWP and IWP are constrained by MWR and RL observations, re-
 488 spectively. The sensitivity of the aerosol DRE to the LWP scaling relationship (Fig. 3a)
 489 (that is used to scale the radar-retrieved LWP when MWR observations are not avail-
 490 able) is tested by using the scaling relationships for all LWC profile (i.e., no collocated
 491 MWR observations are used). The annual mean aerosol DRE differed by 0.01 W m^{-2}
 492 or less, providing confidence that the scaling relationships used are representative in re-
 493 gards to estimating the aerosol DRE. The sensitivity of the LWP scaling relationship (Fig.
 494 3a) is further tested by restricting profiles to those where the MWR LWP is greater than
 495 10 g m^{-2} . The annual mean aerosol DRE differed only by 0.2% (0.1%) at the TOA (sur-
 496 face), showing that the aerosol DRE is insensitive to the opaque cloudy-sky LWP.

497 The sensitivity of the aerosol DRE to the opaque cloudy-sky aerosol profile is also
 498 tested. The monthly mean aerosol extinction profile was used for the heights above where
 499 the RL fully attenuated instead of the weekly mean, which resulted in a difference of 0.01
 500 W m^{-2} at both the TOA and surface. Additionally, the weekly mean aerosol extinction
 501 profile was also used for heights where clouds or precipitation were detected by the radar
 502 instead of considering the aerosol extinction to be zero. The annual mean aerosol DRE
 503 differed by 0.09 (-0.32) W m^{-2} at the TOA (surface), which is -4.3% (5.4%) of the an-
 504 nual mean.

505 5 Aerosol DRE uncertainty estimates associated with measurements

506 In Wu et al. (2021), we estimated the measurement uncertainty and methodology
 507 uncertainty in the estimated clear-sky aerosol DRE. This section focuses on the measure-
 508 ment uncertainty in the estimated all-sky aerosol DRE. See Wu et al. (2021) and Sec-
 509 tion 4.2.1 for the methodology uncertainty. In contrast to the clear-sky aerosol DRE un-
 510 certainty estimates, this study will instead apply the measurement uncertainties to each
 511 model run instead of running one profile for each month with monthly mean climato-
 512 logical aerosol optical properties. For AOD, single-scattering albedo, asymmetry factor,
 513 and surface albedo, the same uncertainty considered for the clear-sky aerosol DRE will
 514 be applied to quantify the all-sky aerosol DRE measurement uncertainty (see Section
 515 6.1.1 in Wu et al. (2021) for specifics). Note that the uncertainty in the single-scattering
 516 albedo is provided for each available AERONET retrieval as a 1-sigma estimate for each
 517 observational wavelength (i.e., 440, 675, 870, and 1020 nm). We derive the mean single-
 518 scattering albedo uncertainty estimate for each wavelength by averaging the individual
 519 single-scattering albedo uncertainty weighted by the optical depth. We then apply this
 520 single-scattering albedo uncertainty interpolated to model wavelengths to estimate the
 521 impact on the aerosol DRE. In addition to aerosol optical properties, measurement un-
 522 certainties associated with clouds due to optical depth, LWP, and particle size will also
 523 be quantified.

524 The annual-mean uncertainty estimates are presented in Table 1. In general, the
 525 relative (absolute) uncertainties in all-sky aerosol DRE due to aerosol optical properties
 526 are similar to those for clear-sky (see Table 1 in Wu et al. (2021)). For example, the an-
 527 nual mean aerosol DRE uncertainty due to AOD is about $\pm 7\text{-}8\%$ at the TOA and the
 528 surface, compared to $\pm 8\%$ for clear-sky. The exception is the uncertainty in the TOA
 529 aerosol DRE due to the aerosol single-scattering albedo, which is 22% in all-sky but 15%
 530 in clear-sky. The single-scattering albedo measurement uncertainty is again the largest
 531 contributor to the measurement uncertainty, which is consistent with McComiskey et al.
 532 (2008), Thorsen et al. (2020), and Thorsen et al. (2021). Compared to clear-sky, the asym-
 533 metry factor and surface albedo measurement uncertainty are slightly higher at the TOA
 534 ($\pm 7\text{-}8\%$) but slightly lower at the surface ($\pm 2\text{-}3\%$).

535 The aerosol DRE uncertainties due to cloud properties measurements are also quan-
 536 tified in Table 1. The cloud measurement uncertainties are separated into those from
 537 the transparent cloudy-sky optical depth, the opaque cloudy-sky LWP, and the opaque
 538 cloudy-sky ice cloud optical depth. For the transparent cloudy-sky optical depth, the mean
 539 relative cloud column optical depth uncertainty is based on the RL-FEX reported ex-
 540 tinction systematic uncertainty, which is found to be $\sim\pm 10\%$, resulting in an uncertainty
 541 in the annual mean aerosol DRE of $\sim 0.01 \text{ W m}^{-2}$ at the TOA and $\sim 0.02 \text{ W m}^{-2}$ at the
 542 surface.

543 For the opaque cloudy-sky LWP, the mean relative uncertainty is based on the MWR-
 544 reported LWP uncertainty of $\pm 10\%$, resulting in the all-sky aerosol DRE uncertainty of
 545 less than 1% at both the TOA and the surface. While the measurement uncertainty in
 546 LWP of $\pm 10\%$ is the uncertainty considered in this study, when considering an uncer-
 547 tainty of $\pm 20\%$ in LWP, the aerosol DRE uncertainty is 2% at the TOA and 1% at the
 548 surface. This further demonstrates that large errors in opaque cloudy-sky LWP does not
 549 impact the aerosol DRE. The opaque cloudy-sky ice cloud optical depth uncertainty is
 550 considered to be similar to that for the transparent ice cloudy-sky condition since the
 551 opaque cloudy-sky IWC profile is scaled using a relationship based on the transparent
 552 RL ice cloud optical depth. The relative uncertainty is $\pm 5\%$, resulting in an uncertainty
 553 in the aerosol DRE of less than 0.1% at the TOA and surface.

554 The liquid cloud particle size uncertainty considered is ± 1.91 microns for trans-
 555 parent cloudy-skies (Thorsen & Fu, 2015a) and $\pm 10\%$ for opaque cloudy-skies (Zhao et
 556 al., 2012). The resulting aerosol DRE uncertainty is 2% at the TOA and 1% at the sur-
 557 face. The ice cloud particle size uncertainty is also considered to be $\pm 10\%$, which results
 558 in an all-sky aerosol DRE uncertainty of less than 1% at both the TOA and the surface.
 559 The small uncertainty in the opaque cloudy-sky terms is expected since the opaque cloudy-
 560 sky contribution is overall very small (Section 4.2).

561 The total aerosol DRE uncertainty estimate associated with measurement uncer-
 562 tainties is quantified in the same manner as Eq. 4 of Wu et al. (2021) by adding the un-
 563 certainties in quadrature, but with additional terms for the uncertainties associated with
 564 the cloud properties. The monthly aerosol DRE with the total monthly measurement
 565 uncertainty is shown in Fig. 9. The monthly relative uncertainty ranges between 20-40%.
 566 Overall, the all-sky aerosol DRE measurement uncertainties are similar to those estimated
 567 for clear-sky despite the additional cloud optical properties uncertainties. All aerosol DRE
 568 uncertainties due to cloud optical properties uncertainty are 2% or less, which are all less
 569 than the smallest clear-sky measurement uncertainty term (3%). In summary we have
 570 annual mean aerosol DREs of -2.13 ± 0.54 ($\mp 25.3\%$) at the TOA and -5.95 ± 0.87 ($\mp 14.5\%$)
 571 at the surface under all-sky conditions, compared to -3.00 ± 0.58 ($\mp 19.4\%$) at TOA and
 572 -6.85 ± 1.00 ($\mp 14.6\%$), respectively, under clear-sky conditions.

573 6 Conclusion

574 The all-sky aerosol direct radiative effects (DREs) were estimated at the Atmospheric
 575 Radiation Measurement Program (ARM) Southern Great Plains (SGP) site using ground-
 576 based observations along with the NASA Langley Fu-Liou radiative transfer model for
 577 the first time. Previously, we quantified the clear-sky aerosol DRE by considering aerosol
 578 optical properties from the Raman lidar and Aerosol Robotic Network (AERONET), at-
 579 mospheric state from radiosondes, and surface shortwave spectral albedo from radiome-
 580 ters. In addition to those observations, cloud extinction vertical profiles from the Ra-
 581 man lidar, cloud water content profiles from the millimeter cloud radar and Ka-band ARM
 582 zenith radar, and cloud liquid water path from the microwave radiometer are also con-
 583 sidered in the all-sky aerosol DRE estimates. Simulated shortwave (SW) downwelling
 584 surface total (F_{total}^{\downarrow}), direct (F_{direct}^{\downarrow}), and diffuse ($F_{diffuse}^{\downarrow}$) fluxes were compared with
 585 observations through a radiative closure experiment for cloudy-sky conditions.

Table 1. The measurement uncertainty (W m^{-2}) in annual mean aerosol direct radiative effect (DRE) under all-sky conditions. The uncertainty is shown for (top) the top of atmosphere (TOA) and (bottom) the surface (SFC) at the Southern Great Plains (SGP) site. The aerosol DRE uncertainty is separated into the uncertainty due to measurement uncertainty of the aerosol optical depth (AOD), column-mean single-scattering albedo ($\bar{\omega}$), column-mean asymmetry factor (\bar{g}), surface albedo (α_s), transparent cloud optical depth ($\tau(\text{cloud, trans.})$), cloud liquid water path (LWP), opaque ice cloud optical depth ($\tau(\text{ice, opaq.})$), liquid cloud particle size (r_e), ice cloud particle size (D_{ge}), and the total uncertainty considering all components. The difference relative to the annual mean aerosol DRE are given in the parentheses.

TOA DRE uncertainty [W m^{-2}]	
AOD	± 0.14 ($\mp 6.7\%$)
$\bar{\omega}$	± 0.47 ($\mp 21.8\%$)
\bar{g}	± 0.15 ($\mp 6.8\%$)
α_s	± 0.18 ($\mp 8.2\%$)
$\tau(\text{cloud, trans.})$	± 0.01 ($\mp 0.5\%$)
LWP	± 0.02 ($\mp 0.8\%$)
$\tau(\text{ice, opaq.})$	± 0.001 ($\mp 0.06\%$)
r_e	± 0.04 ($\mp 1.7\%$)
D_{ge}	± 0.01 ($\mp 0.5\%$)
total	± 0.54 ($\mp 25.3\%$)
SFC DRE uncertainty [W m^{-2}]	
AOD	± 0.45 ($\mp 7.5\%$)
$\bar{\omega}$	± 0.71 ($\mp 12.0\%$)
\bar{g}	± 0.15 ($\mp 2.5\%$)
α_s	± 0.14 ($\mp 2.3\%$)
$\tau(\text{cloud, trans.})$	± 0.02 ($\mp 0.3\%$)
LWP	± 0.02 ($\mp 0.4\%$)
$\tau(\text{ice, opaq.})$	± 0.003 ($\mp 0.04\%$)
r_e	± 0.05 ($\mp 0.8\%$)
D_{ge}	± 0.02 ($\mp 0.3\%$)
total	± 0.87 ($\mp 14.5\%$)

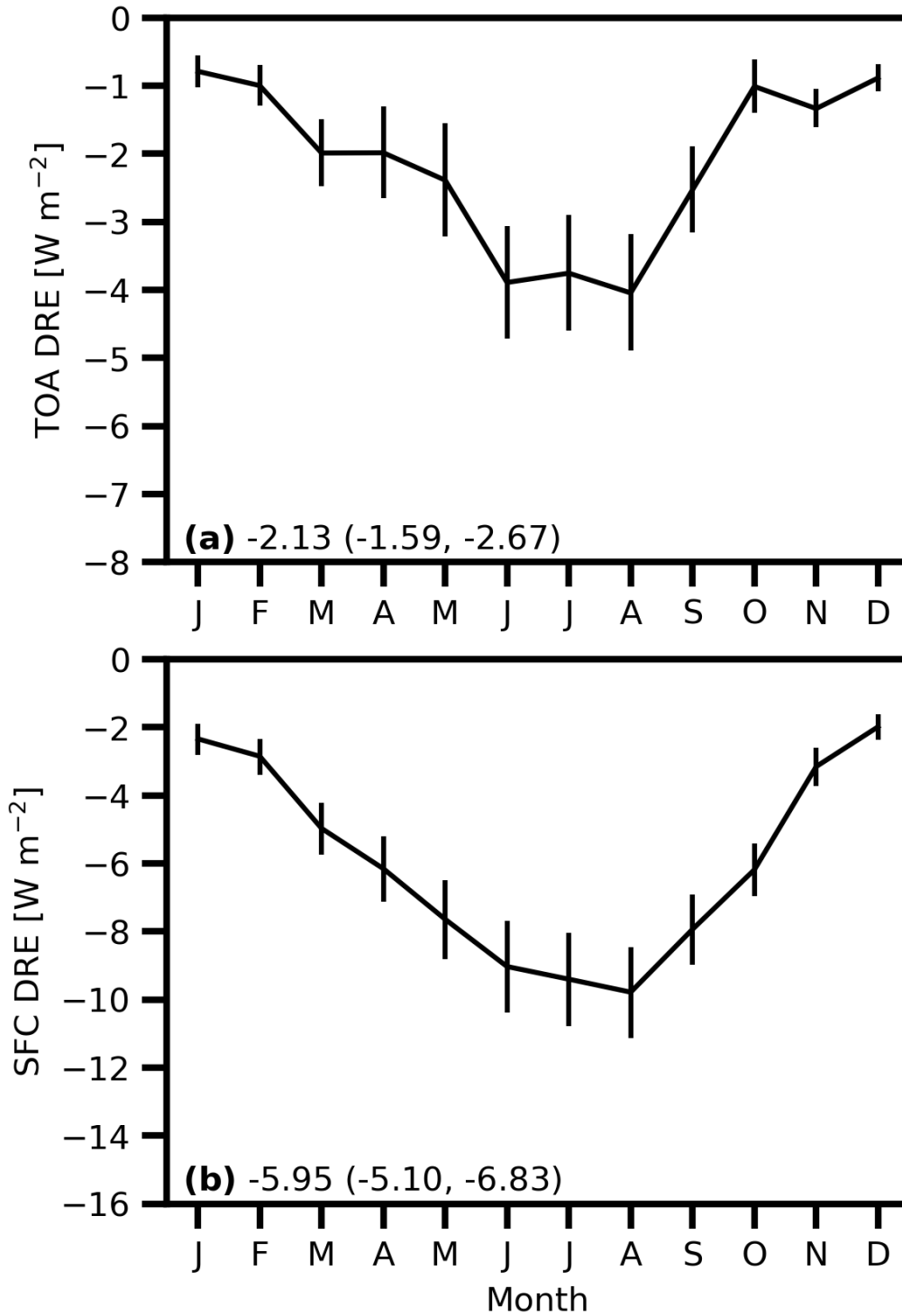


Figure 9. The all-sky aerosol direct radiative effect (DRE) seasonal cycle and the uncertainty estimate (vertical line) due to aerosol optical properties, surface albedo, and cloud properties measurements at the Southern Great Plains (SGP). Results are shown for the (a) top of the atmosphere (TOA) and the (b) surface (SFC). The monthly mean aerosol DRE is the same as those in Fig. 6. The annual mean values are given in the bottom left with the range due to measurement uncertainty in the parentheses.

586 For transparent cloudy-sky profiles, the mean differences between simulated and
 587 observed SW downwelling surface fluxes were 31.85 W m^{-2} (6.0%) for F_{total}^{\downarrow} , 37.71 W
 588 m^{-2} (10.8%) for F_{direct}^{\downarrow} , and -5.87 W m^{-2} (-3.3%) for $F_{diffuse}^{\downarrow}$, which are largely related
 589 to the cloud inhomogeneity and 3D effects. The correlation coefficients between the sim-
 590 ulated and observed fluxes were 0.76 for F_{total}^{\downarrow} , 0.66 for F_{direct}^{\downarrow} , and 0.83 for $F_{diffuse}^{\downarrow}$.
 591 For opaque cloudy-sky profiles, the mean differences between simulated and observed SW
 592 downwelling surface fluxes were -13.23 W m^{-2} (-7.2%) for F_{total}^{\downarrow} and -11.85 W m^{-2} (-
 593 6.5%) for $F_{diffuse}^{\downarrow}$. The correlation coefficients between the simulated and observed fluxes
 594 were 0.86 for F_{total}^{\downarrow} and $F_{diffuse}^{\downarrow}$. These differences become about $1\text{-}2 \text{ W m}^{-2}$ by decreas-
 595 ing the opaque cloud optical depth by 10%.

596 The all-sky aerosol DRE is quantified for the daily mean, monthly mean, and an-
 597 nual mean. In terms of the daily mean, the aerosol DRE ranged from 11.38 to -13.42 W
 598 m^{-2} at the top of the atmosphere (TOA) and from -0.05 to -34.87 W m^{-2} at the sur-
 599 face. In terms of the monthly mean, the aerosol DRE ranged from 2.24 to -5.83 W m^{-2}
 600 at the TOA and -1.27 to -13.75 W m^{-2} at the surface. The annual mean aerosol DRE
 601 was -2.13 W m^{-2} at the TOA and -5.95 W m^{-2} at the surface, which were -3.00 W m^{-2}
 602 and -6.85 W m^{-2} , respectively, under clear-sky conditions for a comparison. Similar to
 603 the clear-sky aerosol DRE estimates in Wu et al. (2021), the seasonal cycle of the all-
 604 sky aerosol DRE largely follows the aerosol optical depth (AOD) seasonal cycle. Addi-
 605 tionally, the solar insolation seasonal cycle amplifies the all-sky aerosol DRE seasonal
 606 cycle. The all-sky aerosol DRE is weaker than the clear-sky aerosol DRE by 28.8% (13.1%)
 607 at the TOA (surface) as the addition of the clouds increases the albedo.

608 The strongest aerosol DREs of -3.90 W m^{-2} at the TOA and -9.41 W m^{-2} at the
 609 surface are during the summer (June-August). The weakest aerosol DREs of -1.01 W
 610 m^{-2} at the TOA and -3.31 W m^{-2} at the surface are in the fall and winter (October-
 611 February). The strongest aerosol DREs correspond to the largest observed AODs while
 612 the weakest aerosol DREs correspond to smaller observed AOD and single-scattering albedo.

613 The all-sky aerosol DRE uncertainty estimates are quantified (Table 1). The mea-
 614 surement uncertainties in aerosol optical properties, surface albedo, and cloud proper-
 615 ties result in the annual mean aerosol DREs of -2.13 ± 0.54 ($\mp 25.3\%$) at the TOA and
 616 -5.95 ± 0.87 ($\mp 14.5\%$) at the surface under all-sky conditions, compared to -3.00 ± 0.58 ($\mp 19.4\%$)
 617 at the TOA and -6.85 ± 1.00 ($\mp 14.6\%$) at the surface, respectively, under clear-sky con-
 618 ditions. The all-sky aerosol DRE relative uncertainty due to individual components is
 619 comparable to that for the clear-sky aerosol DRE except for the aerosol single-scattering
 620 albedo: the uncertainty in the TOA aerosol DRE due to aerosol single-scattering albedo
 621 in all-sky (22%) is larger than that in clear-sky (15%).

622 The regional all-sky aerosol direct radiative effect is quantified from radiative trans-
 623 fer modeling with high-quality ground-based aerosol and cloud observations. The all-sky
 624 aerosol direct radiative effect for one location with a suite of observations can be help-
 625 ful to evaluate the estimated aerosol direct radiative effect from satellite and modeling
 626 efforts, which can further knowledge of aerosols in the climate system and constrain the
 627 aerosol direct radiative forcing, or the radiative perturbation due to anthropogenic aerosol
 628 alone.

629 Acknowledgments

630 The authors thank T.J. Thorsen for useful discussions. The authors also thank R. Marc-
 631 hand and R. Wood for valuable comments and suggestions. This study is supported by
 632 the U.S. Department of Energy Office of Science (BER) under Grant DE-SC0020135.
 633 Data can be downloaded from the AERONET website ([aeronet.gsfc.nasa.gov/new](http://aeronet.gsfc.nasa.gov/new_web/data.html)
 634 [_web/data.html](http://web/data.html)), USGS website (lpdaac.usgs.gov/products/mcd43c1v006/), NOAA
 635 website (www.esrl.noaa.gov/gmd/aggi/aggi.html), and ECMWF website (www.ecmwf
 636 [.int/en/forecasts/datasets/reanalysis-datasets/era-interim](http://int/en/forecasts/datasets/reanalysis-datasets/era-interim)). Data can be down-

637 loaded from the ARM data archive for the Raman lidar ([adc.arm.gov/discovery/#/](http://adc.arm.gov/discovery/#/results/s::rlproffex1thor)
 638 [results/s::rlproffex1thor](http://adc.arm.gov/discovery/#/results/s::sgparsclkazr1kolliasC1)), radar (adc.arm.gov/discovery/#/results/s::sgparsclkazr1kolliasC1),
 639 microwave radiometer (adc.arm.gov/discovery/#/results/s::sgpmwrret1liljclouC1),
 640 and surface flux (adc.arm.gov/discovery/#/results/s::sgpqcrad1longC1).

641 References

- 642 Ackerman, T. P., & Stokes, G. M. (2003). The Atmospheric Radiation Measurement
 643 Program. *Physics Today*, *56*(1), 38–44. Retrieved from [http://physicstoday](http://physicstoday.scitation.org/doi/10.1063/1.1554135)
 644 [.scitation.org/doi/10.1063/1.1554135](http://physicstoday.scitation.org/doi/10.1063/1.1554135) doi: 10.1063/1.1554135
- 645 Balmes, K. A., & Fu, Q. (2018, nov). An Investigation of Optically Very Thin
 646 Ice Clouds from Ground-Based ARM Raman Lidars. *Atmosphere*, *9*(11),
 647 445. Retrieved from <http://www.mdpi.com/2073-4433/9/11/445> doi:
 648 10.3390/atmos9110445
- 649 Balmes, K. A., & Fu, Q. (2020, dec). The diurnally-averaged aerosol direct radiative
 650 effect and the use of the daytime-mean and insolation-weighted-mean solar
 651 zenith angles. *Journal of Quantitative Spectroscopy and Radiative Transfer*,
 652 *257*, 107363. doi: 10.1016/j.jqsrt.2020.107363
- 653 Balmes, K. A., Fu, Q., & Thorsen, T. J. (2019, feb). Differences in Ice Cloud Op-
 654 tical Depth From CALIPSO and Ground-Based Raman Lidar at the ARM
 655 SGP and TWP Sites. *Journal of Geophysical Research: Atmospheres*, *124*(3),
 656 1755–1778. Retrieved from <http://doi.wiley.com/10.1029/2018JD028321>
 657 doi: 10.1029/2018JD028321
- 658 Balmes, K. A., Fu, Q., & Thorsen, T. J. (2021). The diurnal variation of the aerosol
 659 optical depth at the ARM SGP site (submitted). *Earth and Space Science*.
- 660 Bansal, O., Singh, A., & Singh, D. (2019). Aerosol Characteristics over the North-
 661 western Indo-Gangetic Plain: Clear-Sky Radiative Forcing of Composite and
 662 Black Carbon Aerosol. *Aerosol and Air Quality Research*, *19*, 5–14. doi:
 663 10.4209/aaqr.2017.09.0339
- 664 Boucher, O., Randall, D., Artaxo, P., Bretherton, C., Feingold, G., Forster, P., ...
 665 Zhang, X.-Y. (2013). *Clouds and Aerosols*. In T. F. Stocker, et al. (Eds.).
 666 Cambridge, UK. Retrieved from [https://www.ipcc.ch/site/assets/](https://www.ipcc.ch/site/assets/uploads/2018/02/WG1AR5{\\}Chapter07{\\}FINAL-1.pdf)
 667 [uploads/2018/02/WG1AR5{\\}Chapter07{\\}FINAL-1.pdf](https://www.ipcc.ch/site/assets/uploads/2018/02/WG1AR5{\\}Chapter07{\\}FINAL-1.pdf)
- 668 Che, H., Xia, X., Zhao, H., Dubovik, O., Holben, B. N., Goloub, P., ... Zhang,
 669 X. (2019, sep). Spatial distribution of aerosol microphysical and optical
 670 properties and direct radiative effect from the China Aerosol Remote Sensing
 671 Network. *Atmospheric Chemistry and Physics*, *19*(18), 11843–11864. doi:
 672 10.5194/acp-19-11843-2019
- 673 Clothiaux, E. E., Miller, M. A., Turner, D. D., Mace, G. G., Marchand, R. T.,
 674 Widener, K. B., ... Gaustad, K. L. (2001). *The ARM Millimeter Wave Cloud*
 675 *Radars (MMCRs) and the Active Remote Sensing of Clouds (ARSCL) Value*
 676 *Added Product (VAP)* (Tech. Rep.). Washington, DC: U.S. Dep. of Energy.
 677 Retrieved from [https://www.arm.gov/publications/tech{\\}reports/](https://www.arm.gov/publications/tech{\\}reports/arm-vap-002-1.pdf)
 678 [arm-vap-002-1.pdf](https://www.arm.gov/publications/tech{\\}reports/arm-vap-002-1.pdf)
- 679 Comstock, J. M., Protat, A., McFarlane, S. A., Delanoë, J., & Deng, M. (2013,
 680 may). Assessment of uncertainty in cloud radiative effects and heating rates
 681 through retrieval algorithm differences: Analysis using 3 years of ARM data at
 682 Darwin, Australia. *Journal of Geophysical Research: Atmospheres*, *118*(10),
 683 4549–4571. Retrieved from <http://doi.wiley.com/10.1002/jgrd.50404>
 684 doi: 10.1002/jgrd.50404
- 685 Comstock, K. K., Wood, R., Yuter, S. E., & Bretherton, C. S. (2004, oct). Re-
 686 flectivity and rain rate in and below drizzling stratocumulus. *Quarterly Jour-
 687 nal of the Royal Meteorological Society*, *130*(603), 2891–2918. Retrieved from
 688 <http://doi.wiley.com/10.1256/qj.03.187> doi: 10.1256/qj.03.187
- 689 Creekmore, T. N., Joseph, E., Long, C. N., & Li, S. (2014, may). Quantifying

- 690 aerosol direct effects from broadband irradiance and spectral aerosol optical
 691 depth observations. *Journal of Geophysical Research: Atmospheres*, 119(9),
 692 5464–5474. Retrieved from <http://doi.wiley.com/10.1002/2013JD021217>
 693 doi: 10.1002/2013JD021217
- 694 D’Almeida, G. A., Koepke, P., & Shettle, E. P. (1991). *Atmospheric aerosols : global*
 695 *climatology and radiative characteristics*. Hampton, Virginia: A. Deepak.
- 696 Dee, D. P., Uppala, S. M., Simmons, A. J., Berrisford, P., Poli, P., Kobayashi,
 697 S., ... Vitart, F. (2011, apr). The ERA-Interim reanalysis: configura-
 698 tion and performance of the data assimilation system. *Quarterly Journal*
 699 *of the Royal Meteorological Society*, 137(656), 553–597. Retrieved from
 700 <http://doi.wiley.com/10.1002/qj.828> doi: 10.1002/qj.828
- 701 Delene, D. J., & Ogren, J. A. (2002, mar). Variability of aerosol optical properties
 702 at four North American surface monitoring sites. *Journal of the Atmospheric*
 703 *Sciences*, 59(6), 1135–1150. Retrieved from [https://journals.ametsoc.org/
 704 view/journals/atsc/59/6/1520-0469{_}2002{_}059{_}1135{_}](https://journals.ametsoc.org/view/journals/atsc/59/6/1520-0469{_}2002{_}059{_}1135{_}voaopa{_}2.0.co{_}2.xml)
 705 [_}voaopa{_}2.0.co{_}2.xml](https://journals.ametsoc.org/view/journals/atsc/59/6/1520-0469{_}2002{_}059{_}1135{_}voaopa{_}2.0.co{_}2.xml) doi: 10.1175/1520-0469(2002)059<1135:
 706 VOAOPA>2.0.CO;2
- 707 Di Biagio, C., di Sarra, A., & Meloni, D. (2010, may). Large atmospheric short-
 708 wave radiative forcing by Mediterranean aerosols derived from simultaneous
 709 ground-based and spaceborne observations and dependence on the aerosol type
 710 and single scattering albedo. *Journal of Geophysical Research*, 115(D10),
 711 D10209. Retrieved from <http://doi.wiley.com/10.1029/2009JD012697> doi:
 712 10.1029/2009JD012697
- 713 Di Biagio, C., di Sarra, A., Meloni, D., Monteleone, F., Piacentino, S., & Sferlazzo,
 714 D. (2009, mar). Measurements of Mediterranean aerosol radiative forcing
 715 and influence of the single scattering albedo. *Journal of Geophysical Re-*
 716 *search*, 114(D6), D06211. Retrieved from [http://doi.wiley.com/10.1029/
 717 2008JD011037](http://doi.wiley.com/10.1029/2008JD011037) doi: 10.1029/2008JD011037
- 718 Dong, X., Xi, B., & Minnis, P. (2006, may). A climatology of midlatitude con-
 719 tinental clouds from the ARM SGP Central Facility. Part II: Cloud fraction
 720 and surface radiative forcing. *Journal of Climate*, 19(9), 1765–1783. Re-
 721 trieved from [https://journals.ametsoc.org/view/journals/clim/19/9/
 722 jcli3710.1.xml](https://journals.ametsoc.org/view/journals/clim/19/9/jcli3710.1.xml) doi: 10.1175/JCLI3710.1
- 723 Dunn, M., Johnson, K., & Jensen, M. (2011). *The Microbase Value-Added Product:*
 724 *A Baseline Retrieval of Cloud Microphysical Properties* (Tech. Rep.). Washing-
 725 ton, DC: U.S. Dep. of Energy.
- 726 Ferrare, R., Turner, D., Clayton, M., Schmid, B., Redemann, J., Covert, D.,
 727 ... Jonsson, H. (2006, mar). Evaluation of daytime measurements of
 728 aerosols and water vapor made by an operational Raman lidar over the
 729 Southern Great Plains. *Journal of Geophysical Research*, 111(D05S08).
 730 Retrieved from <http://doi.wiley.com/10.1029/2005JD005836> doi:
 731 10.1029/2005JD005836
- 732 Frisch, A. S., Fairall, C. W., & Snider, J. B. (1995, aug). Measurement of Stratus
 733 Cloud and Drizzle Parameters in ASTEX with a K α -Band Doppler Radar
 734 and a Microwave Radiometer. *Journal of the Atmospheric Sciences*, 52(16),
 735 2788–2799. Retrieved from [https://journals.ametsoc.org/view/journals/
 736 atsc/52/16/1520-0469{_}1995{_}052{_}2788{_}moscad{_}2{_}0{_}](https://journals.ametsoc.org/view/journals/atsc/52/16/1520-0469{_}1995{_}052{_}2788{_}moscad{_}2{_}0{_}co{_}2.xml)
 737 [_}co{_}2.xml](https://journals.ametsoc.org/view/journals/atsc/52/16/1520-0469{_}1995{_}052{_}2788{_}moscad{_}2{_}0{_}co{_}2.xml) doi: 10.1175/1520-0469(1995)052<2788:moscad>2.0.co;2
- 738 Fu, Q. (1996, sep). An Accurate Parameterization of the Solar Radiative Properties
 739 of Cirrus Clouds for Climate Models. *Journal of Climate*, 9(9), 2058–2082.
 740 Retrieved from [http://journals.ametsoc.org/doi/abs/10.1175/1520-
 741 0442{_}281996{_}29009{_}3C2058{_}3AAPOTS{_}3E2.0.CO{_}3B2](http://journals.ametsoc.org/doi/abs/10.1175/1520-0442{_}281996{_}29009{_}3C2058{_}3AAPOTS{_}3E2.0.CO{_}3B2)
 742 doi: 10.1175/1520-0442(1996)009<2058:AAPOTS>2.0.CO;2
- 743 Fu, Q., Cribb, M. C., Barker, H. W., Krueger, S. K., & Grossman, A. (2000,
 744 apr). Cloud geometry effects on atmospheric solar absorption. *Jour-*

- 745 *nal of the Atmospheric Sciences*, 57(8), 1156–1168. Retrieved from
 746 <https://journals.ametsoc.org/view/journals/atasc/57/8/1520>
 747 [-0469{_}2000{_}057{_}1156{_}cgeoas{_}2.0.co{_}2.xml](https://doi.org/10.1175/1520-0469(2000)057<1156:CGEOAS>2.0.CO;2) doi:
 748 [10.1175/1520-0469\(2000\)057<1156:CGEOAS>2.0.CO;2](https://doi.org/10.1175/1520-0469(2000)057<1156:CGEOAS>2.0.CO;2)
- 749 Fu, Q., Lesins, G., & Higgins, J. (1999). Aerosol Direct Radiative Forcing : A Five
 750 Year Climatology at the ARM SGP CART Site. In *Ninth arm science team*
 751 *meeting proceedings* (pp. 1994–1997). San Antonio, Texas.
- 752 Fu, Q., & Liou, K. N. (1992, nov). On the Correlated k -Distribution Method
 753 for Radiative Transfer in Nonhomogeneous Atmospheres. *Journal of*
 754 *the Atmospheric Sciences*, 49(22), 2139–2156. Retrieved from [http://](http://journals.ametsoc.org/doi/abs/10.1175/1520-0469(1992)049(2139:OTCDMF)2.0.CO;2)
 755 [journals.ametsoc.org/doi/abs/10.1175/1520-0469{_}281992{_}](http://journals.ametsoc.org/doi/abs/10.1175/1520-0469(1992)049(2139:OTCDMF)2.0.CO;2)
 756 [}29049{_}3C2139{_}3AOTCDMF{_}3E2.0.CO{_}3B2](https://doi.org/10.1175/1520-0469(1992)049(2139:OTCDMF)2.0.CO;2) doi: [10.1175/](https://doi.org/10.1175/1520-0469(1992)049(2139:OTCDMF)2.0.CO;2)
 757 [1520-0469\(1992\)049\(2139:OTCDMF\)2.0.CO;2](https://doi.org/10.1175/1520-0469(1992)049(2139:OTCDMF)2.0.CO;2)
- 758 Fu, Q., & Liou, K. N. (1993, jul). Parameterization of the Radiative Properties
 759 of Cirrus Clouds. *Journal of the Atmospheric Sciences*, 50(13), 2008–2025.
 760 Retrieved from [http://journals.ametsoc.org/doi/abs/10.1175/1520](http://journals.ametsoc.org/doi/abs/10.1175/1520-0469(1993)050(2008:POTRPO)2.0.CO;2)
 761 [-0469{_}281993{_}29050{_}3C2008{_}3APOTRPO{_}3E2.0.CO{_}3B2](https://doi.org/10.1175/1520-0469(1993)050(2008:POTRPO)2.0.CO;2)
 762 doi: [10.1175/1520-0469\(1993\)050\(2008:POTRPO\)2.0.CO;2](https://doi.org/10.1175/1520-0469(1993)050(2008:POTRPO)2.0.CO;2)
- 763 Fu, Q., Yang, P., & Sun, W. B. (1998, sep). An Accurate Parameterization of the
 764 Infrared Radiative Properties of Cirrus Clouds for Climate Models. *Journal of*
 765 *Climate*, 11(9), 2223–2237. Retrieved from [http://journals.ametsoc.org/](http://journals.ametsoc.org/doi/abs/10.1175/1520-0442(1998)011(2223:AAPOTI)2.0.CO;2)
 766 [doi/abs/10.1175/1520-0442{_}281998{_}29011{_}3C2223{_}](https://doi.org/10.1175/1520-0442(1998)011(2223:AAPOTI)2.0.CO;2)
 767 [}3AAAPOTI{_}3E2.0.CO{_}3B2](https://doi.org/10.1175/1520-0442(1998)011(2223:AAPOTI)2.0.CO;2) doi: [10.1175/1520-0442\(1998\)011\(2223:](https://doi.org/10.1175/1520-0442(1998)011(2223:AAPOTI)2.0.CO;2)
 768 [AAPOTI\)2.0.CO;2](https://doi.org/10.1175/1520-0442(1998)011(2223:AAPOTI)2.0.CO;2)
- 769 Fueglistaler, S., & Fu, Q. (2006, dec). Impact of clouds on radiative heating rates
 770 in the tropical lower stratosphere. *Journal of Geophysical Research Atmo-*
 771 *spheres*, 111(23), 23202. Retrieved from [https://agupubs](https://agupubs.onlinelibrary.wiley.com/doi/full/10.1029/2006JD007273)
 772 [.wiley.com/doi/full/10.1029/2006JD007273](https://doi.org/10.1029/2006JD007273)<https://agupubs>
 773 [.onlinelibrary.wiley.com/doi/abs/10.1029/2006JD007273](https://doi.org/10.1029/2006JD007273)[https://](https://agupubs)
 774 [agupubs.onlinelibrary.wiley.com/doi/10.1029/2006JD007273](https://doi.org/10.1029/2006JD007273) doi:
 775 [10.1029/2006JD007273](https://doi.org/10.1029/2006JD007273)
- 776 Gaustad, K. L., Turner, D. D., & McFarlane, S. A. (2011). *MWRRET Value-Added*
 777 *Product: The Retrieval of Liquid Water Path and Precipitable Water Vapor*
 778 *from Microwave Radiometer (MWR) Data Sets* (Tech. Rep.). Washington, DC:
 779 US Dept. of Energy. Retrieved from [https://www.arm.gov/publications/](https://www.arm.gov/publications/tech-reports/doe-sc-arm-tr-081.2.pdf)
 780 [tech{_}reports/doe-sc-arm-tr-081.2.pdf](https://www.arm.gov/publications/tech-reports/doe-sc-arm-tr-081.2.pdf)
- 781 Giles, D. M., Sinyuk, A., Sorokin, M. G., Schafer, J. S., Smirnov, A., Slutsker, I., ...
 782 Lyapustin, A. I. (2019, jan). Advancements in the Aerosol Robotic Network
 783 (AERONET) Version 3 database - automated near-real-time quality control
 784 algorithm with improved cloud screening for Sun photometer aerosol optical
 785 depth (AOD) measurements. *Atmospheric Measurement Techniques*, 12(1),
 786 169–209. doi: [10.5194/amt-12-169-2019](https://doi.org/10.5194/amt-12-169-2019)
- 787 Goldsmith, J. E. M., Blair, F. H., Bisson, S. E., & Turner, D. D. (1998, jul).
 788 Turn-key Raman lidar for profiling atmospheric water vapor, clouds, and
 789 aerosols. *Applied Optics*, 37(21), 4979–4990. Retrieved from [https://](https://www.osapublishing.org/abstract.cfm?URI=ao-37-21-4979)
 790 [www.osapublishing.org/abstract.cfm?URI=ao-37-21-4979](https://doi.org/10.1364/AO.37.004979) doi:
 791 [10.1364/AO.37.004979](https://doi.org/10.1364/AO.37.004979)
- 792 Henderson, D. S., L'Ecuyer, T., Stephens, G., Partain, P., & Sekiguchi, M. (2013,
 793 apr). A Multisensor Perspective on the Radiative Impacts of Clouds and
 794 Aerosols. *Journal of Applied Meteorology and Climatology*, 52(4), 853–871. Re-
 795 trieved from <http://journals.ametsoc.org/doi/10.1175/JAMC-D-12-025.1>
 796 doi: [10.1175/JAMC-D-12-025.1](https://doi.org/10.1175/JAMC-D-12-025.1)
- 797 Hess, M., Koepke, P., & Schult, I. (1998, may). Optical Properties of Aerosols and
 798 Clouds: The Software Package OPAC. *Bulletin of the American Meteorological*
 799 *Society*, 79(5), 831–844. doi: [10.1175/1520-0477\(1998\)079<0831:OPOAAC>2.0](https://doi.org/10.1175/1520-0477(1998)079<0831:OPOAAC>2.0)

800 .CO;2

801 Heymsfield, A., Winker, D., Avery, M., Vaughan, M., Diskin, G., Deng, M., ...

802 Matthey, R. (2014, feb). Relationships between Ice Water Content and
803 Volume Extinction Coefficient from In Situ Observations for Temperatures
804 from 0 to -86C: Implications for Spaceborne Lidar Retrievals. *Journal*
805 *of Applied Meteorology and Climatology*, 53(2), 479–505. Retrieved from
806 <http://journals.ametsoc.org/doi/abs/10.1175/JAMC-D-13-087.1> doi:
807 10.1175/JAMC-D-13-087.1808 Hogan, R. J., Mittermaier, M. P., & Illingworth, A. J. (2006, feb). The retrieval of
809 ice water content from radar reflectivity factor and temperature and its use in
810 evaluating a mesoscale model. *Journal of Applied Meteorology and Climatol-*
811 *ogy*, 45(2), 301–317. Retrieved from [https://journals.ametsoc.org/view/](https://journals.ametsoc.org/view/journals/apme/45/2/jam2340.1.xml)
812 [journals/apme/45/2/jam2340.1.xml](https://journals.ametsoc.org/view/journals/apme/45/2/jam2340.1.xml) doi: 10.1175/JAM2340.1813 Holben, B. N., Eck, T. F., Slutsker, I., Tanré, D., Buis, J. P., Setzer, A., ...
814 Smirnov, A. (1998). AERONET - A federated instrument network and
815 data archive for aerosol characterization. *Remote Sensing*, 66(1), 1–16. doi:
816 10.1016/S0034-4257(98)00031-5817 Iziomon, M. G., & Lohmann, U. (2003). Characteristics and direct radiative effect of
818 mid-latitude continental aerosols: The ARM case. *Atmospheric Chemistry and*
819 *Physics*, 3(6), 1903–1917. doi: 10.5194/acp-3-1903-2003820 Kacenelenbogen, M., Redemann, J., Vaughan, M. A., Omar, A. H., Russell,
821 P. B., Burton, S., ... Hostetler, C. A. (2014, jan). An evaluation of
822 CALIOP/CALIPSO's aerosol-above-cloud detection and retrieval capability
823 over North America. *Journal of Geophysical Research: Atmospheres*, 119(1),
824 230–244. Retrieved from <http://doi.wiley.com/10.1002/2013JD020178>
825 doi: 10.1002/2013JD020178826 Lane, D. E., Goris, K., & Somerville, R. C. (2002, oct). Radiative transfer through
827 broken clouds: Observations and model validation. *Journal of Climate*, 15(20),
828 2921–2933. Retrieved from [https://journals.ametsoc.org/view/journals/](https://journals.ametsoc.org/view/journals/clim/15/20/1520-0442{_}2002{_}015{_}2921{_}rttbco{_}2.0.co{_}2.xml)
829 [clim/15/20/1520-0442{_}2002{_}015{_}2921{_}rttbco{_}2.0.co{_}2](https://journals.ametsoc.org/view/journals/clim/15/20/1520-0442{_}2002{_}015{_}2921{_}rttbco{_}2.0.co{_}2.xml)
830 [.xml](https://journals.ametsoc.org/view/journals/clim/15/20/1520-0442{_}2002{_}015{_}2921{_}rttbco{_}2.0.co{_}2.xml) doi: 10.1175/1520-0442(2002)015(2921:RTTBCO)2.0.CO;2831 Lhermitte, R. (1990, jun). Attenuation and Scattering of Millimeter Wavelength
832 Radiation by Clouds and Precipitation. *Journal of Atmospheric and Oceanic*
833 *Technology*, 7(3), 464–479. Retrieved from [https://journals.ametsoc.org/](https://journals.ametsoc.org/view/journals/atot/7/3/1520-0426{_}1990{_}007{_}0464{_}aasomw{_}2{_}0{_}co{_}2.xml)
834 [view/journals/atot/7/3/1520-0426{_}1990{_}007{_}0464{_}aasomw{_}](https://journals.ametsoc.org/view/journals/atot/7/3/1520-0426{_}1990{_}007{_}0464{_}aasomw{_}2{_}0{_}co{_}2.xml)
835 [_}2{_}0{_}co{_}2.xml](https://journals.ametsoc.org/view/journals/atot/7/3/1520-0426{_}1990{_}007{_}0464{_}aasomw{_}2{_}0{_}co{_}2.xml) doi: 10.1175/1520-0426(1990)007(0464:
836 aasomw)2.0.co;2837 Liao, L., & Sassen, K. (1994, jun). Investigation of relationships between Ka-band
838 radar reflectivity and ice and liquid water contents. *Atmospheric Research*,
839 34(1-4), 231–248. doi: 10.1016/0169-8095(94)90094-9840 Liu, C. L., & Illingworth, A. J. (2000, jul). Toward more accurate retrievals of ice
841 water content from radar measurements of clouds. *Journal of Applied Meteo-*
842 *rology*, 39(7), 1130–1146. Retrieved from [https://journals.ametsoc.org/](https://journals.ametsoc.org/view/journals/apme/39/7/1520-0450{_}2000{_}039{_}1130{_}tmarioi{_}2.0.co{_}2.xml)
843 [view/journals/apme/39/7/1520-0450{_}2000{_}039{_}1130{_}](https://journals.ametsoc.org/view/journals/apme/39/7/1520-0450{_}2000{_}039{_}1130{_}tmarioi{_}2.0.co{_}2.xml)
844 [_}tmarioi{_}2.0.co{_}2.xml](https://journals.ametsoc.org/view/journals/apme/39/7/1520-0450{_}2000{_}039{_}1130{_}tmarioi{_}2.0.co{_}2.xml) doi: 10.1175/1520-0450(2000)039(1130:
845 TMAROI)2.0.CO;2846 Long, C. N., & Shi, Y. (2006). *The QCRad value added product: Surface radiation*
847 *measurement quality control testing, including climatology configurable lim-*
848 *its* (Tech. Rep. No. DOE/SC-ARM/TR-074). Washington, DC: U.S. Dep. of
849 Energy. doi: 10.2172/1019540850 Long, C. N., & Shi, Y. (2008, apr). An Automated Quality Assessment and Control
851 Algorithm for Surface Radiation Measurements. *The Open Atmospheric Sci-*
852 *ence Journal*, 2(1), 23–37. doi: 10.2174/1874282300802010023853 Mace, G. G., & Benson, S. (2008, jun). The vertical structure of cloud occurrence
854 and radiative forcing at the SGP ARM site as revealed by 8 years of continu-

- 855 ous Data. *Journal of Climate*, 21(11), 2591–2610. Retrieved from [https://](https://journals.ametsoc.org/view/journals/clim/21/11/2007jcli1987.1.xml)
856 journals.ametsoc.org/view/journals/clim/21/11/2007jcli1987.1.xml
857 doi: 10.1175/2007JCLI1987.1
- 858 Mace, G. G., Benson, S., & Kato, S. (2006, jun). Cloud radiative forcing at the
859 Atmospheric Radiation Measurement Program Climate Research Facility: 2.
860 Vertical redistribution of radiant energy by clouds. *Journal of Geophysical Re-*
861 *search*, 111(D11), D11S91. Retrieved from [http://doi.wiley.com/10.1029/](http://doi.wiley.com/10.1029/2005JD005922)
862 2005JD005922 doi: 10.1029/2005JD005922
- 863 Mather, J. H., McFarlane, S. A., Miller, M. A., & Johnson, K. L. (2007, mar).
864 Cloud properties and associated radiative heating rates in the tropical
865 western Pacific. *Journal of Geophysical Research*, 112(D5), D05201.
866 Retrieved from <http://doi.wiley.com/10.1029/2006JD007555> doi:
867 10.1029/2006JD007555
- 868 Matus, A. V., L'Ecuyer, T. S., & Henderson, D. S. (2019, jul). New Estimates of
869 Aerosol Direct Radiative Effects and Forcing From ATrain Satellite Obser-
870 vations. *Geophysical Research Letters*, 46(14), 8338–8346. Retrieved from
871 <https://onlinelibrary.wiley.com/doi/10.1029/2019GL083656> doi:
872 10.1029/2019GL083656
- 873 Matus, A. V., L'Ecuyer, T. S., Kay, J. E., Hannay, C., & Lamarque, J.-F. (2015,
874 apr). The Role of Clouds in Modulating Global Aerosol Direct Radia-
875 tive Effects in Spaceborne Active Observations and the Community Earth
876 System Model. *Journal of Climate*, 28(8), 2986–3003. Retrieved from
877 <http://journals.ametsoc.org/doi/10.1175/JCLI-D-14-00426.1> doi:
878 10.1175/JCLI-D-14-00426.1
- 879 McComiskey, A., & Ferrare, R. A. (2016, apr). Aerosol Physical and Optical Prop-
880 erties and Processes in the ARM Program. *Meteorological Monographs*, 57,
881 21.1—21.17. Retrieved from [http://journals.ametsoc.org/mono/article](http://journals.ametsoc.org/mono/article-pdf/doi/10.1175/AMSMONOGRAPHS-D-15-0028.1/3537823/amsmonographs-d-15-0028%5B%5D.pdf)
882 -[pdf/doi/10.1175/AMSMONOGRAPHS-D-15-0028.1/3537823/amsmonographs-d-](http://journals.ametsoc.org/mono/article-pdf/doi/10.1175/AMSMONOGRAPHS-D-15-0028.1/3537823/amsmonographs-d-15-0028%5B%5D.pdf)
883 -15-0028%5B%5D.pdf doi: 10.1175/amsmonographs-d-15-0028.1
- 884 McComiskey, A., Schwartz, S. E., Schmid, B., Guan, H., Lewis, E. R., Ricchiazzi, P.,
885 & Ogren, J. A. (2008, may). Direct aerosol forcing: Calculation from observ-
886 ables and sensitivities to inputs. *Journal of Geophysical Research*, 113(D9),
887 D09202. Retrieved from <http://doi.wiley.com/10.1029/2007JD009170> doi:
888 10.1029/2007JD009170
- 889 Michalsky, J. J., Anderson, G. P., Barnard, J., Delamere, J., Gueymard, C., Kato,
890 S., ... Ricchiazzi, P. (2006). Shortwave radiative closure studies for clear
891 skies during the Atmospheric Radiation Measurement 2003 Aerosol Inten-
892 sive Observation Period. *Journal of Geophysical Research*, 111(D14S90).
893 Retrieved from <http://doi.wiley.com/10.1029/2005JD006341> doi:
894 10.1029/2005JD006341
- 895 Miller, M. A., & Slingo, A. (2007, aug). The ARM Mobile Facility and its first inter-
896 national deployment: Measuring radiative flux divergence in West Africa. *Bul-*
897 -*letin of the American Meteorological Society*, 88(8), 1229–1244. doi: 10.1175/
898 BAMS-88-8-1229
- 899 Min, Q.-L., Duan, M., & Marchand, R. (2003, sep). Validation of surface retrieved
900 cloud optical properties with in situ measurements at the Atmospheric Radia-
901 tion Measurement Program (ARM) South Great Plains site. *Journal of Geo-*
902 -*physical Research*, 108(D17), 4547. Retrieved from [http://doi.wiley.com/](http://doi.wiley.com/10.1029/2003JD003385)
903 10.1029/2003JD003385 doi: 10.1029/2003JD003385
- 904 Mortier, A., Goloub, P., Derimian, Y., Tanré, D., Podvin, T., Blarel, L., ... Ndi-
905 -*aye, T.* (2016, jun). Climatology of aerosol properties and clear-sky short-
906 -*wave radiative effects using Lidar and Sun photometer observations in the*
907 -*Dakar site.* *Journal of Geophysical Research: Atmospheres*, 121(11), 6489–
908 -*6510.* Retrieved from <http://doi.wiley.com/10.1002/2015JD024588> doi:
909 10.1002/2015JD024588

- 910 Newsom, R. K. (2009). *Raman Lidar (RL) Handbook* (Tech. Rep.). Wash-
 911 ington, DC: U.S. Dep. of Energy. Retrieved from [https://www.arm.gov/
 912 publications/tech{_}reports/handbooks/rl{_}handbook.pdf](https://www.arm.gov/publications/tech{_}reports/handbooks/rl{_}handbook.pdf)
- 913 Oikawa, E., Nakajima, T., & Winker, D. (2018, jan). An Evaluation of the Short-
 914 wave Direct Aerosol Radiative Forcing Using CALIOP and MODIS Obser-
 915 vations. *Journal of Geophysical Research: Atmospheres*, *123*(2), 1211–1233.
 916 Retrieved from [https://onlinelibrary.wiley.com/doi/abs/10.1002/
 917 2017JD027247](https://onlinelibrary.wiley.com/doi/abs/10.1002/2017JD027247) doi: 10.1002/2017JD027247
- 918 Omar, A. H., Winker, D. M., Tackett, J. L., Giles, D. M., Kar, J., Liu, Z., ...
 919 Trepte, C. R. (2013, may). CALIOP and AERONET aerosol optical depth
 920 comparisons: One size fits none. *Journal of Geophysical Research: At-
 921 mospheres*, *118*(10), 4748–4766. Retrieved from [http://doi.wiley.com/
 922 10.1002/jgrd.50330](http://doi.wiley.com/10.1002/jgrd.50330) doi: 10.1002/jgrd.50330
- 923 Oyola, M. I., Campbell, J. R., Xian, P., Bucholtz, A., Ferrare, R. A., Burton, S. P.,
 924 ... Lolli, S. (2019, jan). Quantifying the direct radiative effect of absorbing
 925 aerosols for numerical weather prediction: A case study. *Atmospheric Chem-
 926 istry and Physics*, *19*(1), 205–218. doi: 10.5194/acp-19-205-2019
- 927 Reddy, M. S., Boucher, O., Balkanski, Y., & Schulz, M. (2005, jun). Aerosol optical
 928 depths and direct radiative perturbations by species and source type. *Geophys-
 929 ical Research Letters*, *32*(L12803). Retrieved from [http://doi.wiley.com/10
 930 .1029/2004GL021743](http://doi.wiley.com/10.1029/2004GL021743) doi: 10.1029/2004GL021743
- 931 Redemann, J., Vaughan, M. A., Zhang, Q., Shinozuka, Y., Russell, P. B., Liv-
 932 ington, J. M., ... Remer, L. A. (2012). The comparison of MODIS-Aqua
 933 (C5) and CALIOP (V2 & V3) aerosol optical depth. *Atmospheric Chemistry
 934 and Physics*, *12*(6), 3025–3043. doi: 10.5194/acp-12-3025-2012
- 935 Roesch, A., Schaaf, C. B., & Gao, F. (2004, jun). Use of Moderate-Resolution
 936 Imaging Spectroradiometer bidirectional reflectance distribution function
 937 products to enhance simulated surface albedos. *Journal of Geophysical Re-
 938 search*, *109*(D12), D12105. Retrieved from [http://doi.wiley.com/10.1029/
 939 2004JD004552](http://doi.wiley.com/10.1029/2004JD004552) doi: 10.1029/2004JD004552
- 940 Rogers, R. R., Vaughan, M. A., Hostetler, C. A., Burton, S. P., Ferrare, R. A.,
 941 Young, S. A., ... Winker, D. M. (2014, dec). Looking through the haze: Eval-
 942 uating the CALIPSO level 2 aerosol optical depth using airborne high spectral
 943 resolution lidar data. *Atmospheric Measurement Techniques*, *7*(12), 4317–4340.
 944 doi: 10.5194/amt-7-4317-2014
- 945 Rose, F., Charlock, T., Fu, Q., Kato, S., Rutan, D., & Jin, Z. (2006). CERES
 946 Proto-edition 3 radiative transfer: Model tests and radiative closure over
 947 surface validation sites. In A. M. Society (Ed.), *12th conf. on atmospheric
 948 radiation, amer. meteor. soc.* (p. P2.4). Madison, WI. Retrieved from
 949 <https://ams.confex.com/ams/pdfpapers/112358.pdf>
- 950 Rose, F. G., & Charlock, T. P. (2002). New Fu-Liou Code Tested with ARM Raman
 951 Lidar Aerosols and CERES In Pre-CALIPSO Sensitivity Study. In A. M. So-
 952 ciety (Ed.), *11th conference on atmopsheric radiation* (p. P4.8). Ogden, UT.
 953 Retrieved from [https://ams.confex.com/ams/11AR11CP/techprogram/
 954 paper{_}42757.htm](https://ams.confex.com/ams/11AR11CP/techprogram/paper{_}42757.htm)
- 955 Schaaf, C. B., Gao, F., Strahler, A. H., Lucht, W., Li, X., Tsang, T., ... Roy,
 956 D. (2002, nov). First operational BRDF, albedo nadir reflectance prod-
 957 ucts from MODIS. *Remote Sensing of Environment*, *83*(1-2), 135–148. doi:
 958 10.1016/S0034-4257(02)00091-3
- 959 Sherman, J. P., & McComiskey, A. (2018, mar). Measurement-based climatology of
 960 aerosol direct radiative effect, its sensitivities, and uncertainties from a back-
 961 ground southeast US site. *Atmospheric Chemistry and Physics*, *18*(6), 4131–
 962 4152. Retrieved from [https://www.atmos-chem-phys.net/18/4131/2018/
 963 doi: 10.5194/acp-18-4131-2018](https://www.atmos-chem-phys.net/18/4131/2018/)
- 964 Shupe, M. D., Turner, D. D., Zwink, A., Thieman, M. M., Mlawer, E. J., Ship-

- 965 pert, T., ... Shippert, T. (2015, jul). Deriving Arctic Cloud Microphysics
 966 at Barrow, Alaska: Algorithms, Results, and Radiative Closure. *Journal*
 967 *of Applied Meteorology and Climatology*, 54(7), 1675–1689. Retrieved from
 968 <http://journals.ametsoc.org/doi/10.1175/JAMC-D-15-0054.1> doi:
 969 10.1175/JAMC-D-15-0054.1
- 970 Thorsen, T. J., Ferrare, R. A., Hostetler, C. A., Vaughan, M. A., & Fu, Q. (2017,
 971 sep). The impact of lidar detection sensitivity on assessing aerosol di-
 972 rect radiative effects. *Geophysical Research Letters*, 44(17), 9059–9067.
 973 Retrieved from <http://doi.wiley.com/10.1002/2017GL074521> doi:
 974 10.1002/2017GL074521
- 975 Thorsen, T. J., Ferrare, R. A., Kato, S., & Winker, D. M. (2020, jul). Aerosol Di-
 976 rect Radiative Effect Sensitivity Analysis. *Journal of Climate*, 33(14), 6119–
 977 6139. Retrieved from [https://journals.ametsoc.org/view/journals/clim/](https://journals.ametsoc.org/view/journals/clim/33/14/JCLI-D-19-0669.1.xml)
 978 [33/14/JCLI-D-19-0669.1.xml](https://journals.ametsoc.org/view/journals/clim/33/14/JCLI-D-19-0669.1.xml) doi: 10.1175/JCLI-D-19-0669.1
- 979 Thorsen, T. J., & Fu, Q. (2015a, nov). Automated Retrieval of Cloud and Aerosol
 980 Properties from the ARM Raman Lidar. Part II: Extinction. *Journal of*
 981 *Atmospheric and Oceanic Technology*, 32(11), 1999–2023. Retrieved from
 982 <http://journals.ametsoc.org/doi/10.1175/JTECH-D-14-00178.1> doi:
 983 10.1175/JTECH-D-14-00178.1
- 984 Thorsen, T. J., & Fu, Q. (2015b, dec). CALIPSO-inferred aerosol direct radiative
 985 effects: Bias estimates using ground-based Raman lidars. *Journal of Geophys-*
 986 *ical Research: Atmospheres*, 120(23), 12,209–12,220. Retrieved from [http://](http://doi.wiley.com/10.1002/2015JD024095)
 987 doi.wiley.com/10.1002/2015JD024095 doi: 10.1002/2015JD024095
- 988 Thorsen, T. J., Fu, Q., & Comstock, J. M. (2013, jun). Cloud effects on radia-
 989 tive heating rate profiles over Darwin using ARM and A-train radar/lidar
 990 observations. *Journal of Geophysical Research: Atmospheres*, 118(11), 5637–
 991 5654. Retrieved from <http://doi.wiley.com/10.1002/jgrd.50476> doi:
 992 10.1002/jgrd.50476
- 993 Thorsen, T. J., Fu, Q., Newsom, R. K., Turner, D. D., & Comstock, J. M.
 994 (2015, nov). Automated Retrieval of Cloud and Aerosol Properties from
 995 the ARM Raman Lidar. Part I: Feature Detection. *Journal of Atmo-*
 996 *spheric and Oceanic Technology*, 32(11), 1977–1998. Retrieved from
 997 <http://journals.ametsoc.org/doi/10.1175/JTECH-D-14-00150.1> doi:
 998 10.1175/JTECH-D-14-00150.1
- 999 Thorsen, T. J., Winker, D. M., & Ferrare, R. A. (2021, jan). Uncertainty in obser-
 1000 vational estimates of the aerosol direct radiative effect and forcing. *Journal of*
 1001 *Climate*, 34(1), 195–214. Retrieved from [https://doi.org/10.1175/JCLI-D-](https://doi.org/10.1175/JCLI-D-19-01009.1)
 1002 [-19-](https://doi.org/10.1175/JCLI-D-19-01009.1) doi: 10.1175/JCLI-D-19-01009.1
- 1003 Turner, D. D., Vogelmann, A. M., Austin, R. T., Barnard, J. C., Cady-Pereira, K.,
 1004 Chiu, J. C., ... Wiscombe, W. (2007, feb). *Thin liquid water clouds: Their*
 1005 *importance and our challenge* (Vol. 88) (No. 2). American Meteorological Soci-
 1006 ety. Retrieved from [https://journals.ametsoc.org/view/journals/bams/](https://journals.ametsoc.org/view/journals/bams/88/2/bams-88-2-177.xml)
 1007 [88/2/bams-88-2-177.xml](https://journals.ametsoc.org/view/journals/bams/88/2/bams-88-2-177.xml) doi: 10.1175/BAMS-88-2-177
- 1008 Wood, R. (2005, sep). Drizzle in stratiform boundary layer clouds. Part II: Mi-
 1009 crophysical aspects. *Journal of the Atmospheric Sciences*, 62(9), 3034–3050.
 1010 Retrieved from [https://journals.ametsoc.org/view/journals/atsc/62/9/](https://journals.ametsoc.org/view/journals/atsc/62/9/jas3530.1.xml)
 1011 [jas3530.1.xml](https://journals.ametsoc.org/view/journals/atsc/62/9/jas3530.1.xml) doi: 10.1175/JAS3530.1
- 1012 Wu, X., Balmes, K. A., & Fu, Q. (2021, mar). Aerosol Direct Radiative Ef-
 1013 fects at the ARM SGP and TWP Sites: Clear Skies. *Journal of Geo-*
 1014 *physical Research: Atmospheres*, 126(5), e2020JD033663. Retrieved from
 1015 <https://onlinelibrary.wiley.com/doi/10.1029/2020JD033663> doi:
 1016 10.1029/2020JD033663
- 1017 Xia, X., Che, H., Zhu, J., Chen, H., Cong, Z., Deng, X., ... Zhang, X. (2016, jan).
 1018 Ground-based remote sensing of aerosol climatology in China: Aerosol opti-
 1019 cal properties, direct radiative effect and its parameterization. *Atmospheric*

1020
1021
1022
1023
1024
1025
1026
1027
1028
1029
1030
1031
1032
1033
1034

- Environment*, 124, 243–251. doi: 10.1016/j.atmosenv.2015.05.071
- Yu, H., Dickinson, R. E., Chin, M., Kaufman, Y. J., Zhou, M., Zhou, L., ... Holben, B. N. (2004, feb). Direct radiative effect of aerosols as determined from a combination of MODIS retrievals and GOCART simulations. *Journal of Geophysical Research*, 109(D03206). doi: 10.1029/2003jd003914
- Yu, H., Kaufman, Y. J., Chin, M., Feingold, G., Remer, L. A., Anderson, T. L., ... Zhou, M. (2006, feb). A review of measurement-based assessments of the aerosol direct radiative effect and forcing. *Atmospheric Chemistry and Physics*, 6(3), 613–666. Retrieved from <http://www.atmos-chem-phys.net/6/613/2006/> doi: 10.5194/acp-6-613-2006
- Zhao, C., Xie, S., Klein, S. A., Protat, A., Shupe, M. D., McFarlane, S. A., ... Wang, Z. (2012, may). Toward understanding of differences in current cloud retrievals of ARM ground-based measurements. *Journal of Geophysical Research: Atmospheres*, 117(D10206). Retrieved from <http://doi.wiley.com/10.1029/2011JD016792> doi: 10.1029/2011JD016792